

# Noise Filtering and Optical Readout for Quantum Circuit Electromechanics

Master's Thesis

submitted in partial fulfillment of the requirements for the  
BS-MS Dual Degree

by

**Yash J Joshi**



**EPFL**

Indian Institute of Science Education and  
Research Pune  
Dr. Homi Bhabha Road,  
Pashan, Pune 411008, India.

École Polytechnique Fédérale de Lausanne  
Station 3 - Lausanne 1015  
Switzerland

April, 2020

Supervisor: Dr. Tobias J Kippenberg

© Yash J Joshi 2020

All rights reserved



Physics is too hard to be left to physicists.


— David Hilbert

This thesis is dedicated to my parents.



# Certificate

This is to certify that this dissertation entitled “Noise Filtering and Optical Readout for Quantum Circuit Electromechanics” towards the partial fulfilment of the BS-MS dual degree programme at the Indian Institute of Science Education and Research, Pune represents the work carried out by Yash J Joshi, at École Polytechnique Fédérale de Lausanne (EPFL), CH-1015 Lausanne, Switzerland, under the supervision of Dr. Tobias J. Kippenberg, Full Professor, Institute of Physics, during the academic year 2019-2020.



Dr. Tobias J. Kippenberg

**Committee:**

Dr. Tobias J. Kippenberg

Dr. Bijay Agarwalla



# Declaration

I hereby declare that the matter embodied in the report entitled “Noise Filtering and Optical Readout for Quantum Circuit Electromechanics”, is the results of the work carried out by me at the Institute of Physics, École Polytechnique Fédérale de Lausanne (EPFL), CH-1015 Lausanne, Switzerland, under the supervision of Prof. Tobias J. Kippenberg, and the same has not been submitted elsewhere for any other degree.



Yash J. Joshi



# Acknowledgements

I want to start by thanking Prof. Tobias Kippenberg, who gave me this wonderful opportunity to pursue a masters thesis in his lab. The environment that he has cultivated in his lab, with a world class team and laboratory equipment, was greatly conducive to my academic as well as personal growth during the past year for which I cannot thank him enough.

I want to thank Nathan Bernier for teaching me tips and tricks of microwave superconducting experiments and for theoretical discussions that help me understand the subject better. I thank Amir Youssefi and Itay Shomroni for leading and directing the projects in the lab that I enjoyed working on. I want to thank Nick Sauerwein and Philipp Urich for initiating the filter cavity project. Especially Nick, who even after graduating from the Kippenberg lab, still invested a lot of time for continuous discussions with me and even machined some parts of the system with me to take this project to completion. I also want to thank Amirali, Alberto, Nils, Mohammed, Miles, and Philippe for interesting lunchtable conversations and Arslan and Anat for some entertaining cross-border banter. I want to thank Antonella Ragnelli and Kathleen Vionnet for helping me sort out my administrative queries, purchase lab equipment and for organising two scientific conferences that I benefited from.

I want to thank Dr. Bijay Agarwalla for introducing me to the field of cavity optomechanics. I also want to thank Dr Bhas Bapat, Dr Sudarshan Ananth, and Dr Seema Sharma for discussions and their guidance on academic and scientific life. I want to thank Dr Chaitanya Athale for my brief exploration of mathematical biology.

This thesis is the culmination of 5 years of undergraduate studies. So it only makes sense to acknowledge the friends who made this journey more enjoyable and survivable. I want to thank Rohit, Sourabh, Raj, Kaustubh and Sujeet for interesting debates and Saturday night outs; Prerana, Sriram, Arindam and Prasanna for always being there for me; good folks from physics mimamsa such as Rugved, Lakshya, Nandini, Avik, Rahul with whom I enjoyed discussing physics; the iGEM team, particularly Aarti and Avani, for the great Boston adventure; Abhishek,



Niramay, Sreelakshmi, and Anwasha for always entertaining me. I grateful to have become friends with David, Jørgen, Rachel, Leonie, and Sina who made my time in Switzerland more fun and for pushed me to do things outside my comfort zone.

*Lausanne, 20 March 2020*

Yash Joshi

# Abstract

Circuit electromechanics and Josephson junction based superconducting qubits are two experimental fields that have generated vast attention in the past decade. This thesis aims at solving some experimental challenges in dealing with these systems. The phase noise of microwave sources is an issue that plagues these experiments and custom built filter cavities are used to reduce the phase noise by tuning it to a particular frequency. In this work, a system of a filter cavity and two motors was assembled, and a program based on the Nelder-Mead minimisation algorithm was written to tune the filter cavity to any arbitrary frequency by looking at its response on a network analyser. Tuning with the frequency space accuracy of 50 kHz, and extinction of around 20-30 dB is demonstrated. The second challenge that was addressed was the readout of weak signals from the superconducting devices at cryogenic temperatures. As the conventionally used HEMT amplifiers and coaxial cables contribute to a significant heat load, we instead implement LiNbO<sub>3</sub> electro-optic phase modulator, connected to room temperature heterodyne detection setup by optical fibers of lower thermal conductivity. The characterisation of the phase modulator was done by measuring its half-wave voltage at cryogenic temperatures. Observation of optomechanically induced transparency and parametric instability was demonstrated using both the conventional HEMT readout as well as EOM-based optical readout.

Key words: cavity optomechanics, circuit electromechanics, quantum engineering



# Contents

<b>Acknowledgements</b>	<b>v</b>
<b>Abstract</b>	<b>vii</b>
<b>List of figures</b>	<b>xi</b>
<b>1 Introduction</b>	<b>1</b>
1.1 Circuit electromechanics . . . . .	1
1.1.1 Classical description of Electromechanics . . . . .	1
1.1.2 Quantum model of electromechanics . . . . .	5
1.1.3 Experimental setup . . . . .	5
1.2 Noise in circuit electromechanical experiments . . . . .	5
1.2.1 Resolved sideband cooling . . . . .	5
1.2.2 Phase noise . . . . .	8
1.3 Optical Readout of superconducting electromechanical systems . . . . .	9
1.3.1 Superconducting qubits scalability . . . . .	10
1.3.2 Optical interconnects . . . . .	11
<b>2 Filtering the phase noise</b>	<b>13</b>
2.1 Phase noise of the microwave sources . . . . .	13
2.2 Tunable filter cavity . . . . .	13
2.3 Need for automation . . . . .	15
2.4 Cavity design . . . . .	16
2.5 Characterisation . . . . .	16
2.6 Brute force algorithm for Tuning . . . . .	18
2.6.1 Tunability with the brute force algorithm . . . . .	18
2.7 Filtering the phase noise . . . . .	20
2.8 Failure of the brute force algorithm . . . . .	21

2.9	Nelder-Mead algorithm . . . . .	23
2.9.1	Tunability with the nelder mead algorithm . . . . .	23
2.9.2	Benchmarking the Coarse tunability . . . . .	24
2.10	Conclusion . . . . .	26
<b>3</b>	<b>Optical readout of cryogenic superconducting systems</b>	<b>27</b>
3.1	Lithium-Niobate modulators . . . . .	27
3.2	Experimental setup . . . . .	28
3.2.1	Heterodyne detection . . . . .	29
3.2.2	Pound-Drevor-Hall frequency locking . . . . .	29
3.3	Measurement of half-wave voltage . . . . .	30
3.3.1	Caliberation of Microwave power reaching the EOM . . . . .	31
3.3.2	Temperature dependence of the half-wave voltage . . . . .	33
3.3.3	Frequency dependence at cryogenic temperatures . . . . .	34
3.4	Investigating heating due to Optical power dissipation . . . . .	35
3.5	Performance of an Amplitude moduator at cryogenic temperatures . . . . .	36
3.5.1	Data transmission . . . . .	37
3.6	Optical readout of optomechanically induced transparency . . . . .	38
3.7	Observation of the parametric instability . . . . .	39
3.8	Conclusion . . . . .	40
<b>4</b>	<b>Conclusion and Outlook</b>	<b>43</b>
	<b>Bibliography</b>	<b>47</b>

# List of Figures

1.1	Schematic of a circuit electromechanical system . . . . .	2
1.2	Transmission of the cavity depending on the input-output coupling . . . . .	3
1.3	Schematic of experimental setup . . . . .	6
2.1	Total noise and the phase noise of the microwave source . . . . .	14
2.2	Rendering and image of the filter cavity . . . . .	15
2.3	Schematic of experimental setup for characterisation of the filter cavity . . . . .	16
2.4	Characterisation and performance of the filter cavity . . . . .	17
2.5	Fine tunability of the system with the brute force algorithm . . . . .	19
2.6	Accuracy and Precision of the tuning algorithm . . . . .	20
2.7	Phase noise filtering . . . . .	21
2.8	Parameter space and function to be minimised . . . . .	22
2.9	Coarse tunability of the system with Nelder-mead algorithm . . . . .	24
2.10	Fine tunability of the system with Nelder-mead algorithm . . . . .	24
2.11	Coarse tunability of the system over 20 iterations . . . . .	25
2.12	Q factors of the fitted resonances . . . . .	25
3.1	Experimental setup for electro-optic readout . . . . .	29
3.2	Insertion loss in the coaxial cables . . . . .	32
3.3	Calibrated insertion loss at cryogenic temperatures . . . . .	33
3.4	Measurement of $V_\pi$ vs Temperature . . . . .	34
3.5	Frequency dependence of the $V_\pi$ . . . . .	35
3.6	Heating in the cryostat due to optical dissipation . . . . .	35
3.7	Temperature dependence of transmission of an amplitude modulator . . . . .	36
3.8	Data transmission experiment for an amplitude modulator . . . . .	37
3.9	Electro-optic readout of optomechanically induced transparency . . . . .	39
3.10	Electro-optic readout of optomechanical parametric instability . . . . .	40



# 1 Introduction

The theory of quantum mechanics has been extensively studied and verified on electronic, atomic and even ionic scale by many experiments during the 20th century. Cavity optomechanics [1] has emerged as a novel experimental scheme that attempts to probe the quantum nature of a macroscopic objects. In this scheme, an optical (or a microwave) cavity is coupled to a mechanical harmonic oscillator, in such a way that mechanical position changes the cavity length and thus the resonant frequency and the light in optical cavity exerts a radiation pressure force on the mechanical oscillator. This scheme can be realised in many different experiments of vastly different length-scales, examples range from microtoroids with whispering gallery modes, photonic crystals, soft clamped membrane in the middle system, to the optical cavities with kg-scale test masses in the LIGO experiment.

## 1.1 Circuit electromechanics

In this thesis, our optomechanical system of interest is a superconducting electromechanical device. In its quantum optical treatment, an optical cavity can simply be thought of as an harmonic oscillator. Therefore, any electromagnetic system that can be described as a harmonic oscillator can be treated as an optical cavity. In our case, this role of an optical cavity is played by an LC resonator. The role of a mechanical harmonic oscillator is played by one of the capacitor plates that has a mechanical mode. Figure 1.1 shows this schematic.

### 1.1.1 Classical description of Electromechanics

Let us first consider a simple LC circuit. We consider the voltage across the capacitor ( $V_C = Q/C$ ) and the inductor ( $V_L = L \frac{dI}{dt}$ ), and apply the Kirchoff's law-  $V_C + V_L = 0$ . This allows us to describe the circuit as a simple harmonic oscillator of resonant frequency of  $\omega_c = \frac{1}{\sqrt{LC}}$ . If we consider



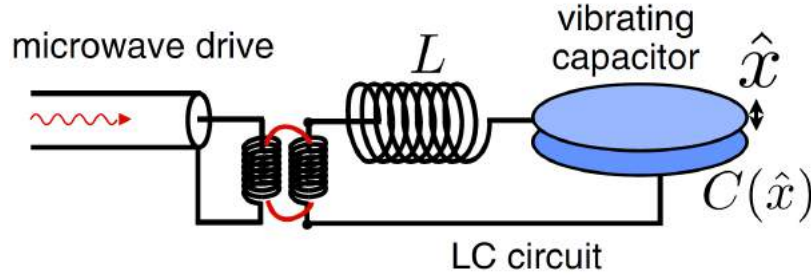


Figure 1.1 – Schematic of a circuit electromechanical system. Image taken from Ref. [1]

the charge on the capacitor as the variable of interest, the equation of motion is

$$\frac{d^2 Q}{dt^2} = -\omega_c^2 Q$$

We can go to the complex space and reduce the above second order differential equation, to two first order differential equations by defining  $a_{\pm} = \frac{1}{\sqrt{2C}}(Q \mp i\sqrt{LC}I)$ , where the choice of normalisation constant  $\frac{1}{\sqrt{2C}}$  is chosen such that  $|a|^2$  gives us the total intracavity energy ( $= \frac{Q^2}{2C} + \frac{1}{2}LI^2$ ). The resulting equations are-

$$\frac{da_+}{dt} = i\omega_c a_+ \quad \text{and} \quad \frac{da_-}{dt} = -i\omega_c a_-$$

Since the two equations are complex conjugates of each other, it suffices to describe the system only with one of them, so we redefine  $a_+ = a$ . This formalism is highly useful, as apart from reducing the order of differential equation, when we go to the quantum picture, the variables  $a_+$  and  $a_-$  will become the ladder operators  $a$  and  $a^\dagger$ , already familiar to us in the treatment of a quantum harmonic oscillator.

Now if we introduce losses and consider a source that is driving the harmonic oscillator, we can get the equation-

$$\frac{da}{dt} = i\omega_c a - \frac{\kappa}{2}a + \sqrt{\kappa_{\text{ex}}}\bar{s}e^{i\omega_L t} \quad (1.1)$$

Where we assumed that there are two channels for dissipation, one internal ( $\kappa_0$ ) and one that via the input-output coupling to the waveguide ( $\kappa_{\text{ex}}$ ). The total dissipation rate is  $\kappa = \kappa_0 + \kappa_{\text{ex}}$ , and it can be shown from time-reversibility arguments that the input coupling coefficient should be equal to  $\sqrt{\kappa_{\text{ex}}}$  [2].

### Input-Output theory

We can solve this equation using the integration factor method to obtain an expression for the intracavity field-

$$a = \frac{\sqrt{\kappa_{\text{ex}}}\bar{s}e^{i\omega_L t}}{i(\omega_L - \omega_c) + \kappa/2} \quad (1.2)$$

We will denote  $\Delta = \omega_L - \omega_c$  from here onward, as optical detuning of the drive field. Since only the amplitude of the field is of interest, we can go to the rotating frame and rewrite above equations as-

$$\frac{da}{dt} = -i\Delta a - \frac{\kappa}{2}a + \sqrt{\kappa_{\text{ex}}}\bar{s} \quad \text{and} \quad a = \frac{\sqrt{\kappa_{\text{ex}}}\bar{s}}{i\Delta + \kappa/2} \quad (1.3)$$

From the same time reversibility conditions, we can also obtain the input-output relation between the incoming wave incident on the cavity with amplitude  $s$  and the transmitted wave going out of the cavity with amplitude  $t$ -

$$t = s - \sqrt{\kappa_{\text{ex}}}a \quad (1.4)$$

The transmission coefficient  $|\frac{t}{s}|^2$  can be obtained from the equations 1.4 and 1.2. The transmission depends greatly on the coupling conditions of the cavity to the waveguide. The transmission is shown in the following figure 1.2

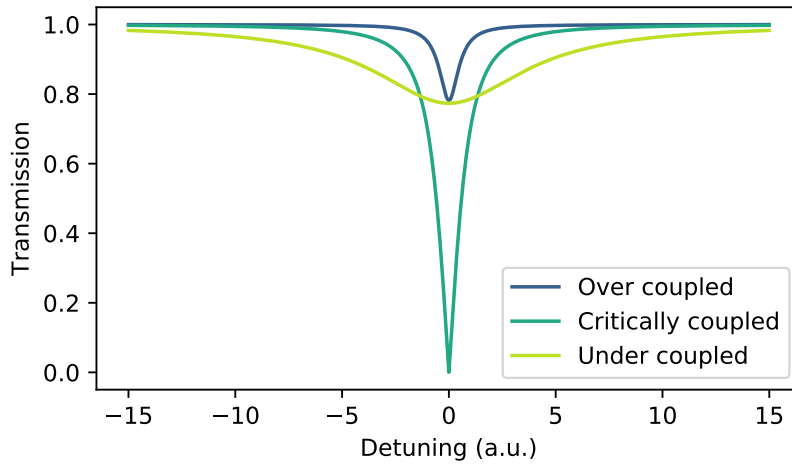


Figure 1.2 – Transmission of the cavity for different conditions of the input-output coupling

This plot can be explained heuristically as follows- If the system is ‘Over-coupled’,  $\kappa_{\text{ex}} \gg \kappa_0$ , then the photons that flow into the cavity does not have sufficient time to dissipate, and are sent back to the waveguide. If the system is ‘under-coupled’, i.e.  $\kappa_{\text{ex}} \ll \kappa_0$ , then the photons do not flow into the cavity efficiently. If however, the system is critically coupled, i.e.  $\kappa_{\text{ex}} = \kappa_0$ , then we

get that the transmission  $\rightarrow 0$  as detuning  $\rightarrow 0$ . This condition will become important when we discuss tuning the filter cavities in the chapter 2.

### Electromechanical coupling

Now, we divert our attention to the optomechanical coupling. Let us consider that the capacitor has a capacitance  $C = \epsilon_0 A/d$ . We consider that one of the capacitor plates can execute its own mechanical simple harmonic motion, around the relaxed position of gap distance 'd', This in turn changes the capacitance ( $C = \epsilon_0 A/d + x$ ). Thus, the resonant frequency of the circuit depends on the position of the mechanical oscillator as

$$\omega = \frac{1}{\sqrt{LC}} = \sqrt{\frac{d+x}{L\epsilon_0 A}} = \frac{1}{\sqrt{LC}} \left(1 + \frac{x}{d}\right)^{\frac{1}{2}} = \omega_c \left(1 + \frac{x}{2d}\right) = \omega_c + Gx$$

Where we define  $G = \omega_c/2d$  to be the electromechanical coupling. This describes the action of the mechanical motion on the microwave mode of the LC circuit. To describe the action of the microwave mode on the mechanics, we consider the force on the capacitor plate, which depends on the charge. To write it in terms of  $a$ , we use  $Q = \sqrt{2C}(a_+ + a_-)$  to get-

$$F_c = -\frac{Q^2}{2Cd} = -\frac{2C(a_+ + a_-)^2}{2Cd} = -\frac{(a_+^2 + a_-^2 + 2a_+a_-)}{d} \approx -\frac{2|a|^2}{d} = -4\frac{G}{\omega_c}|a|^2 \quad (1.5)$$

Where the terms  $a_+^2$  and  $a_-^2$  are ignored under the *Rotating wave approximation*, because they are rotating with twice the microwave frequency, which is much higher than the frequency of mechanics hence they are seen as their cycle averaged value, which is zero. The negative sign of the force denotes that the force is attractive, i.e. it acts in the direction opposite to the positive x axis.

We substitute this back into the (1.1) and together with an equation for the harmonic motion of the mechanical oscillator, we obtain the set of two equations that describe our electromechanical system-

$$\frac{da}{dt} = -i(\Delta - Gx)a - \frac{\kappa}{2}a + \sqrt{\kappa_{ex}}s \quad (1.6)$$

$$m\frac{d^2x}{dt^2} = -m\Omega_m^2x - m\Gamma_m\frac{dx}{dt} - 4\frac{G}{\omega_c}|a|^2 + F_L(t) \quad (1.7)$$

Where,  $\omega_L$  denotes the frequency of microwave or optical signal with which drives the cavity,  $m$  is the mass of harmonic oscillator,  $\Omega_m$  is the frequency of the mechanical mode that interacts

with the optical mode,  $\Gamma_m$  is the mechanical damping rate,  $F_L(t)$  is the thermal langevin force that satisfies the time uncorrelation condition-  $\langle F_L(t)F_L(t') \rangle = m\Gamma_m k_B T \delta(t-t')$ .

### 1.1.2 Quantum model of electromechanics

The Hamiltonian of an isolated quantum optomechanical system can be written as-

$$H = \hbar\omega_c a^\dagger a + \hbar\Omega_m b^\dagger b + \hbar g_0 a^\dagger a (b^\dagger + b). \quad (1.8)$$

where,  $a$  denotes the lowering operator for the optical resonant mode of the cavity,  $b$  denotes the lowering operator for the mechanical resonant mode of the harmonic oscillator, and  $g_0$  represents the bare optomechanical coupling rate.

### 1.1.3 Experimental setup

An ideal LC circuit has no resistance. To achieve this, we need to cool down our sample to the temperatures where they are superconducting. To be able to do experiments that show the quantum nature of our harmonic oscillators, we need to be able to isolate the system well enough from the environment. For this purpose we use a cryogenic dilution refrigerator that can cool our samples to the temperatures of about 15 mK. The figure 1.3 shows the schematic of a typical circuit electromechanics experimental setup.

Microwave signal generators are used to send microwave tones via coaxial copper cables to the circuit electromechanical device under test. The reflected signal is amplified by a HEMT amplifier to detect the weak signal coming from the device. The VNA is used to measure the response of the circuit electromechanical system and find resonances in the circuit. The ESA is used to measure the signals scattered by the device.

## 1.2 Noise in circuit electromechanical experiments

In this section, the basic theory of optomechanics, notably the resolved sideband cooling of the mechanical motion will be reviewed and the effect of the phase noise of the input optical source will be investigated theoretically.

### 1.2.1 Resolved sideband cooling

When we drive our cavity with a red detuned microwave pump, the intracavity light field can act as an additional damping reservoir and can extract energy from the mechanical motion. To see this we need to solve the equations of motion 1.6 and 1.7. To solve these equation, we make an assumption  $\Omega_m \gg \kappa$ , i.e. the mechanical frequency is much greater than cavity

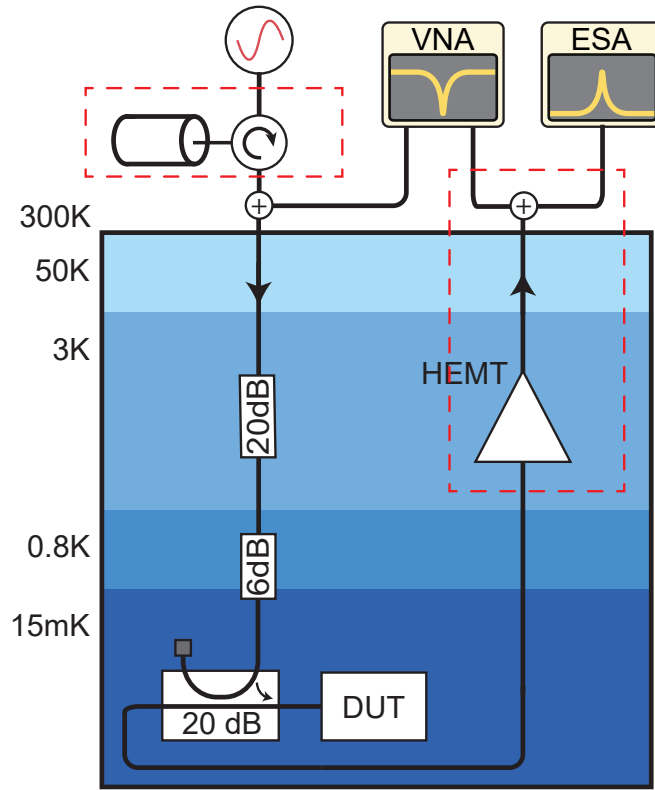


Figure 1.3 – Schematic of the experimental setup for measurement of a circuit electromechanical system. The red dashed box shows the parts of the experiment that this thesis focuses on.

linewidth. This condition is known as the “Resolved sideband” condition, due to the fact that if a microwave tone is sent to the cavity at resonance, the mechanics modulates the phase of the incoming light and sidebands are generated at one mechanical frequency away from the tone, and these sidebands lie outside the cavity linewidth. Considering different timescales of the system, the physical implication of this assumption is that since the cavity dissipation rate is much lower, the intracavity field does not change significantly over one period of mechanical motion, which allows for the perturbative treatment followed. This assumption holds true for the circuit electromechanical samples that we work with, in which the mechanical frequency is  $\Omega_m \sim 2\pi \times 5 - 10$  MHz and the cavity linewidth is  $\kappa \sim 2\pi \times 0.3 - 0.8$  MHz.

We assume steady state condition for the mechanical oscillator, ignore the Langevin force and assume the solution of the equation 1.7 to be  $x(t) = x_0 \cos(\Omega_m t)$ . To solve the equation 1.6, we assume there to be a steady state, and a perturbation around this steady state caused by the mechanical motion, i.e.  $a = a_0 + a_1(t)$ . Substituting this in the equation 1.6, cancelling out terms of  $a_0$  and ignoring the term proportional to  $xa_1$  since it is of second order in perturbation,

we get-

$$\frac{da_1}{dt} = -iGx_0 \cos(\Omega_m t) a_0 - \left(i\Delta + \frac{\kappa}{2}\right) a_1$$

Writing the cosine in terms of exponentials and solving the above equation by the integrating factor method, we get-

$$a_1 = iGx_0 a_0 \left[ \frac{e^{i\Omega_m t}}{i(\Delta + \Omega_m) + \frac{\kappa}{2}} + \frac{e^{-i\Omega_m t}}{i(\Delta - \Omega_m) + \frac{\kappa}{2}} \right]$$

where the value of  $a_0$  has been established in the section 1.1.1 to be  $a_0 = \frac{\sqrt{\kappa_{ex} \delta}}{i\Delta + \kappa/2}$ .

Now we write the total intracavity field, assuming drive tone to be red detuned by one mechanical frequency, i.e.  $\Delta = -\Omega_m$ , resulting in

$$a = a_0 \left( 1 + iGx_0 \frac{e^{i\Omega_m t}}{\kappa/2} \right) \quad (1.9)$$

The force on the capacitor plate can be given by-

$$F_c = -4 \frac{G}{\omega_c} |a|^2 = -4 \frac{G}{\omega_c} |a_0|^2 \left( 1 + iGx_0 \frac{e^{i\Omega_m t}}{\kappa/2} \right) \left( 1 - iGx_0 \frac{e^{-i\Omega_m t}}{\kappa/2} \right) \approx 16 \frac{G^2}{\omega_c} |a_0|^2 x_0 \sin(\Omega_m t)$$

Ignoring the constant term.

Hence, we get a force acting on the mechanical oscillator, which is proportional to  $\sin(\Omega_m t)$ . By substituting this back to the right hand side of the equation of motion for the harmonic oscillator, equation 1.7, we can see that this force modifies the damping rate of the harmonic oscillator -

$$F_{tot} = -m\Omega_m^2 x_0 \cos(\Omega_m t) + m\Gamma_m x_0 \sin(\Omega_m t) + 16 \frac{G^2}{\omega_c} |a_0|^2 x_0 \sin(\Omega_m t)$$

In the above equation, we can see that the radiation pressure force,  $F_c$  is merely modifying the mechanical damping factor. Hence, we can rewrite the total damping factor as-

$$\Gamma_{tot} = \Gamma_m + \Gamma_{opt} \quad (1.10)$$

Alternatively, we can consider the power imparted by this force on the mechanical motion, which can be expressed as  $\langle P_m \rangle = \langle F_c(t) \dot{x} \rangle$ . Since the  $F_c$  is positive and the derivative of  $x$  carries a negative sign, we get the average value of the power over one cycle to be negative.

This clearly shows that the radiation pressure force due to the electromechanical coupling,

extract the energy from the mechanical oscillator and thus effectively “cools” it. This is known in the literature as “Optomechanical cooling due to dynamical backaction”, since the effect can be described as the modification of mechanical dynamics caused by a response of the optical field to changes in the cavity size. It is also called “Resolved sideband cooling”, due to the condition that we imposed in the derivation above.

The notion of “cooling” will be more clear if we consider the quantum picture of a harmonic oscillator. An oscillator thermalised to its environmental temperature  $T$  will have a phonon occupancy given by the Bose occupation factor  $n_{th} = (e^{\hbar\omega/k_B T} - 1)^{-1}$ . When we drive the cavity on the red detuned side, the anti-stokes process, in which the incoming photon absorbs a phonon and is scattered into a photon of higher frequency, is enhanced whereas the stokes process is suppressed. Since this causes the extinction of phonons, the phonon occupancy is lowered. In this case, the light field can be thought of as the environment of lower temperature to which the harmonic oscillator now thermalises. Using this technique, it has been demonstrated in the circuit electromechanical systems [3], that harmonic oscillator can be brought to phonon occupancies of  $n_{th} \sim 0.34$  or in other words, cooled to its ground state

### 1.2.2 Phase noise

In the above section, we have assumed the input tone to be an ideal delta peaked wave at only one frequency, i.e.  $s = e^{i\omega_L t}$ . However, this is rarely the case in any realistic experimental setting. The microwave signal generator in our experiment, or even lasers used in optomechanical experiments have significant phase noise. The phase noise at one mechanical frequency away from the tone can beat with the tone and cause the heating of our mechanical oscillator and put a lower limit on how much we can cool the system. To see how the phase noise can cause heating, we follow the treatment given in ref. [4].

Considering that our signal, instead of being an ideal signal, has a phase modulation of depth  $\beta$  at the frequency of one mechanical linewidth away from the tone, i.e.

$$s(t) = s e^{i\omega_L t} \left( 1 + \beta e^{i\Omega_m t} - \beta e^{-i\Omega_m t} \right) \quad (1.11)$$

Next, we again need to solve the equation 1.1 in the rotating frame to obtain the intracavity field. Excluding the electromechanical contribution, for red detuned tone,  $\Delta = -\Omega_m$  it can be written as-

$$a = a_0 + \sqrt{\kappa_{\text{ex}}} s \frac{\beta e^{i\Omega_m t}}{\kappa/2} \quad (1.12)$$

Assuming deeply sideband resolved regime,  $\Omega_m \gg \kappa$ , the expression for steady state intracavity

field simplifies to  $a_0 = \frac{\sqrt{\kappa_{\text{ex}} s}}{-i\Omega_m}$ . We can now write the expression for force on the mechanical oscillator to be -

$$F_c = -4 \frac{G}{\omega_c} |a|^2 = -4G \left( \frac{\sqrt{\kappa_{\text{ex}} s}}{-i\Omega_m} + \sqrt{\kappa_{\text{ex}} s} \beta \frac{e^{i\Omega_m t}}{\kappa/2} \right) \left( \frac{\sqrt{\kappa_{\text{ex}} s}}{i\Omega_m} + \sqrt{\kappa_{\text{ex}} s} \beta \frac{e^{-i\Omega_m t}}{\kappa/2} \right) \quad (1.13)$$

$$= -4 \frac{G}{\omega_c} |s|^2 \frac{\beta}{\Omega_m} \sin(\Omega_m t) \quad (1.14)$$

Where we have ignored the time independent (constant) terms. We can see that we get a negative term for the force. Since it is negative, it implies that this force reduces the value of the damping factor  $\Gamma_m$  or alternatively, it implies that the average power imparted on the mechanical oscillator over one cycle is positive and hence, the oscillator will be driven by this force.

Due to this reason, laser phase noise is a significant hurdle when it comes to optomechanical cooling of the mechanical oscillators to its ground state. So much so that the calculated value of lowest achievable phonon occupancy was  $n = 5000$  for the experiment of [4]. This problem needs to be addressed for effective sideband cooling of the oscillator.

As a solution to this problem of phase noise, Copper filter cavities are commonly used in many optomechanical experiments [3, 5, 6]. These cavities are tuned specifically so that one of their resonant modes lies exactly one mechanical mode frequency away from the microwave tone. This results in the phase noise at the frequency  $\omega_L + \Omega_m$  being reduced to the shot noise level of the source, depending on how well the filter cavity is tuned. In the above papers, these filter cavities are often custom-designed and built. They also need to be manually tuned a certain frequency each time a measurement is to be taken with the microwave tone at a particular frequency. The aim of this project was to standardise a design for these filter cavities and assemble a system that can make the filter cavity automatically tunable. So that every time a measurement needs to be taken, a simple command can be given to the computer and the filter cavity will be tuned to the desired frequency

### 1.3 Optical Readout of superconducting electromechanical systems

In our experiment, the input lines to the superconducting device under test (DUT) have in total 46 dB of attenuation. After the signal interacts and reflects from the DUT, we want to detect it. However, at the room temperature ( $T \sim 293K$ ), the thermal noise in the number of quanta for a 5 GHz signal is given by  $k_B T / \hbar \omega \approx 1200$  quanta. This sets a lower bound on the strength of the signal in number of photons that can be detected directly. In an ideal case, our goal would be to



be able to measure signals that are quantum limited, i.e. the noise floor would correspond to  $\bar{n}_{th} + 1/2$  quanta. For this reason, we need to use amplifiers, that can amplify the signal so that thermal noise is not a limitation. An amplifier at cryogenic temperature can amplify the signal coming from the device so much that addition of thermal noise to this signal does not matter.

Suppose we have a signal coming from the device at 15 mK stage, with the spectral density  $S_{\hat{a}\hat{a}}(\omega)$ . A linear amplifier is usually characterised by two parameters, its gain  $G$  and the noise it adds to the signal,  $N_{add}$ . Quantitatively, any amplifier can be modelled in terms of spectral densities as-

$$S^{out}[\omega] = G(S^{in}[\omega] + N_{add})$$

If two amplifiers of  $(G_1, N_1)$  and  $(G_2, N_2)$  are added sequentially, then the total gain and added noise can be calculated as follows-

$$S_1^{out}[\omega] = G_1(S_0^{in}[\omega] + N_1)$$

$$S_2^{out}[\omega] = G_2(S_1^{in}[\omega] + N_2) = G_1G_2S_0^{in}[\omega] + G_2(G_1N_1 + N_2)$$

Since the value of gain is usually very high,  $G_1N_1 \gg N_2$ , and hence the noise in the second amplifier does not matter.

In all experiments with cryogenic superconducting circuits, most commonly used amplifiers are the HEMT (High Electron Mobility Transistors) based amplifiers. Typically, HEMT amplifiers have around 10 – 15 quanta of added noise at the temperature of 3K.

### 1.3.1 Superconducting qubits scalability

Recent advances in superconducting quantum circuits [7–9] have highlighted the potential associated with scaling superconducting qubit technology [10]. Currently, significant efforts are underway to scale the number of qubits. As a result, one of the challenges that future progress in superconducting circuits will face is to massively increase the number of microwave control and readout lines while preserving the base temperature and protecting qubits from thermal noise.

Typically copper coaxial cables are used to connect the HEMT at 3 K to room temperature amplifier and measurement instruments such as VNA and ESA. This leads to significant heat load exacerbated by the high thermal conductivity of the cables. This proves to be a challenge for the development of scalable superconducting qubit systems and the heat load per qubit needs to be reduced.

In contrast to copper coaxial cables ( $> 1$  dB/km), optical fibers exhibit ultralow-loss optical propagation ( $\sim 0.2$  dB/km). In addition, the thermal conductivity of silica,  $\sim 0.1$  W/(m K),

makes optical fibers excellent thermal insulators compared to copper cables, which have the thermal conductivity of the order of 100 W/(m K). Optical fibers could therefore provide a solution to scaling the number drive lines without the adding significant heat load.

### 1.3.2 Optical interconnects

For this approach involving optical fibers, a critical component are modulators which convert input microwave signals to the optical domain, that are compatible with low temperature operation and are sufficiently efficient to ensure low noise (quantum-limited) transduction of microwave to optical signals.

Indeed, substantial efforts are underway to create quantum coherent interfaces between the microwave and optical domains. To date, quantum coherent conversion schemes based on piezoelectromechanical [11, 12], magneto-optical [13], and optomechanical [14–16] coupling have been developed. In addition, schemes based on cavity electro-optics [17] have been demonstrated using bulk [18, 19], and integrated [20] microwave cavities coupled via the Pockel's effect of an optical cavity mode. Yet, all these schemes have in common that they transduce narrow-band microwave signals to the optical domain. While this ability is critical for future quantum networks, an optical replacement for the currently employed HEMT amplifiers may be required for scaling control lines. One route is therefore to use broadband optical modulators as already used today in telecommunication networks.

In this project, we explore this potential to replace the HEMT amplifier with a LiNbO<sub>3</sub>-based optical phase modulator (PM), in order to directly transduce the DUT microwave output signal onto sidebands around the optical carrier field, detectable using standard homodyne or heterodyne detection schemes at ambient temperatures. In contrast to electrical amplifiers, electro-optical modulators require no electrical power and can operate with low optical loss. The dependence electro-optic effect and optical loss on temperature, down to 600 mK is investigated. The electro-optic transduction is also demonstrated at low temperatures to show the effective transduction of microwave signals into optical signals, to observe the electromechanical effects via optical detection.



## 2 Filtering the phase noise

As has been elaborated in the previous chapter, the phase noise of the microwave sources is of great concern in the circuit electromechanical experiments. In this chapter, I will investigate this phase noise, describe the design and characterisation of the copper filter cavities that we use to filter out the phase noise at desired frequencies. I will describe the automation of the task of tuning the filter cavities and various algorithms used to achieve it, as well as the mechanical modifications of the system.

### 2.1 Phase noise of the microwave sources

In this section, the phase noise of the microwave sources used for the circuit electromechanics experiments will be investigated. For this purpose, I use an a Rhode & Shwarz Signal and Spectrum Analyser (FSW-26), that provides the phase noise measurement. The microwave source used here is Keysight MXG X-Series Signal Generator N5183B, and we generate a microwave tone at  $\omega = 2\pi \times 5$  GHz and 10 dBm in power.

When a microwave tone of frequency  $\omega$  is sent to the FSW via a coaxial cable, the FSW locks onto the tone and follows long-timescale deviations in the frequency and the amplitude of the tone so as to accurately measure the spectrum of noise around the range of a few MHz in the frequency domain. The FSW can independently measure the total noise and phase noise by rejecting the amplitude noise. The figure 2.1 shows the noise characteristics of our source.

### 2.2 Tunable filter cavity

For the purpose of removing the phase noise of the source at a given frequency, cylindrical copper cavities are commonly used in experiments [5, 6]. The microwave tone from the source is sent through a circulator to the filter cavity. If the frequency of the incoming signal is off-resonant, the signal is simply reflected. If however, the signal is of resonant frequency, there is

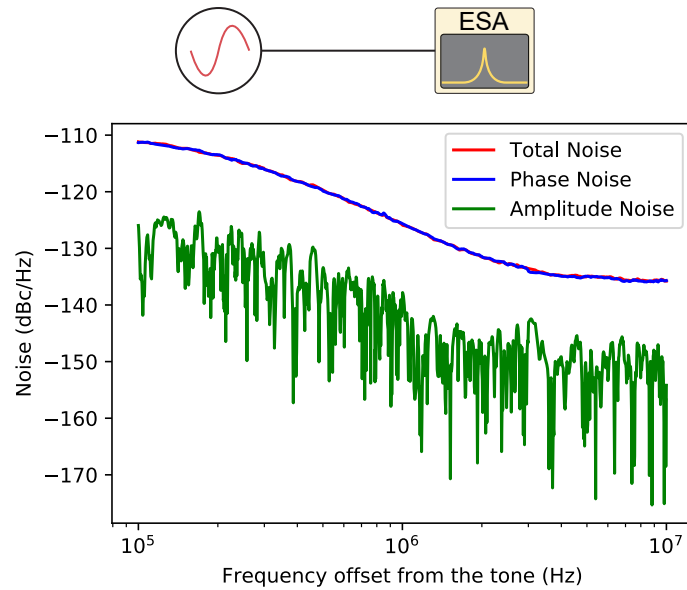


Figure 2.1 – Total noise and the phase noise of the microwave source around the tone of frequency 5GHz

constructive interference inside the cavity and the energy of the signal is stored in the cavity. Now, there are two channels of dissipation for this energy, one is through the internal losses of the cavity  $\kappa_0$  and one is via the input-output coupling of the cavity to the microwave waveguide  $\kappa_{ex}$ . If  $\kappa_0 < \kappa_{ex}$ , then it means that the energy is not dissipated sufficiently fast from the cavity via the internal channel and it is just sent back to the waveguide. If on the other hand,  $\kappa_0 > \kappa_{ex}$ , it means that most of the signal is not entering the cavity at all and it is only getting reflected. Hence, for the maximum absorption of our signal, the critical coupling condition  $\kappa_0 = \kappa_{ex}$  has to be achieved. Hence, for the accurate tuning of the filter cavities, two parameters have to be optimized- resonance frequency  $\omega_k$  (of an arbitrary 'k'th mode) and external coupling rate  $\kappa_{ex}$ .

We designed a system of a cylindrical copper cavity with a movable piston and two motors. The first motor is connected to a linear stage which can move in a single direction up to a distance of 50mm. (Zaber motorised linear stage X-LSM050A). This motor is connected to the piston that fits inside the cylindrical cavity with a few Thorlabs optomechanical components. This setup allows us to change the length of the cavity and thus change the frequency of the resonant modes of the cavity. The rendering and a picture of the filter cavity setup is shown in the Figure 2.2.

The microwave signal is fed into the cavity by means of a small copper cable that acts as an antenna. The antenna is designed so that it makes a small angle with respect to the axis of the cylinder and its base is away from the center of the circular cross section of the cylinder. The

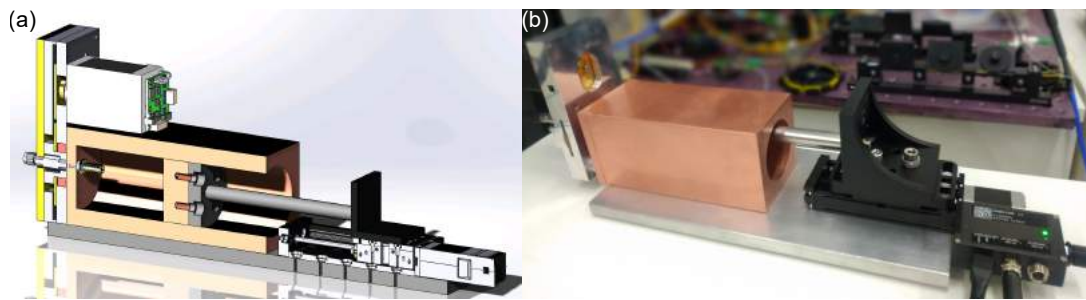


Figure 2.2 – **Rendering and picture of the setup:** (a) shows the SolidWorks rendering of the cross section of the filter cavity. (b) shows the actual image of the setup

second motor (Trinamic stepper motor PD42-1-1140) is used to rotate the antenna, such that its tip follows a circular path inside the cavity. Turning the motor to rotate the antenna allows us to control the external coupling rate  $\kappa_{\text{ex}}$  of the cavity to the microwave waveguide.

The schematic of our experimental setup is shown in the 2.3. For measuring and tuning the filter cavity, the microwave source is kept off and only look at the response of the filter cavity using the Rhode & Schwarz Vector Network Analyser (ZNB20). The amplitude of the scattering parameter ( $S_{21}$ ) shows a dip at resonant frequencies and it's phase shows a sigmoidal curve described by the input-output theory. The VNA trace is read by the computer running a python script, and according to the algorithm described in the next section, moves the two motors to tune the filter cavity to desired frequency.

## 2.3 Need for automation

In many optomechanical experiments, such as ponderomotive squeezing [21], the frequency of optical source is varied around the cavity frequency by the order of few MHz. Optomechanical squeezing below the shot noise level is observed as a dip at the frequencies when the detuning is equal to the frequency of the mechanical mode. Now if we want to do these detuning sweeps, everytime we change the frequency by a small amount (order of  $\sim 1$  MHz), we need to tune the filter cavity at one mechanical mode frequency away from the microwave tone. In the previous manual design of the filter cavity, tuning it by hand, places a lower limit on how fine a detuning sweep we can do and how many data points we can obtain. To get rid of this constraint, an automisation algorithm is required so that for every data point, the algorithm takes the corresponding frequency at which the phase noise should be knocked out as the input and then tunes the filter cavity to this frequency without need of any manual setting.

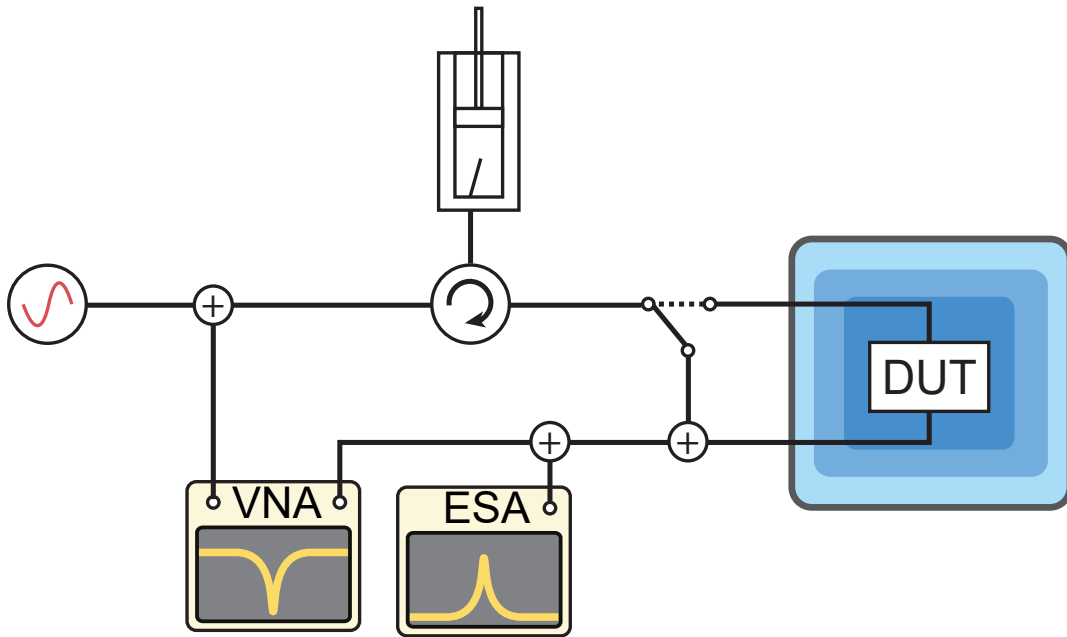


Figure 2.3 – Schematic of experimental setup for characterisation of the filter cavity. Dotted lines indicate the configuration to be used for filtering noise in the circuit electromechanical experiments performed on the ‘DUT’ at cryogenic temperatures

## 2.4 Cavity design

By solving the Maxwell’s equations for the cylindrical cavity, the dependence of frequencies of various resonant modes on the length and radius of the cavity can be found to be-

$$\omega_{nlm} = c \sqrt{\left(\frac{\alpha_{nl}}{R}\right)^2 + \left(\frac{m\pi}{L}\right)^2} \quad (2.1)$$

Where,  $c$  is the speed of light,  $\alpha_{nl}$  is the  $l$ -th zero of (the derivative of) the order  $n$  Bessel function of first kind ( $J'_n J_n$  for the (TE) TM mode,  $R$  is the radius of the cylindrical cavity and  $L$  is the length of the filter cavity. Just as TE and TM modes have different frequencies, they also have a field distribution that signify constructive and destructive interference of incoming waves. These distributions are often axially symmetric, and this is exactly the property exploited while designing the antenna to be off-center.

## 2.5 Characterisation

We wanted to know within the frequency domain of our interest, i.e. 4 GHz - 9 GHz, where the resonant modes of the cavity are situated, and how do they move upon changing the length of the

cavity. We can see from the figure 2.4 (a) that the frequency of a resonant mode increases with decreasing the length of the cavity, and the functional dependence matches the theoretical values obtained by Equation 2.1. Next, we use the algorithm for detecting resonances, as described in the previous paragraph, and apply it to this data and the results are shown in the figure 2.4(b). We can also compare this result with the length dependence of resonant frequencies given by equation 2.1 and we can see in figure 2.4(b) that our results match quite well with the theory, and most of the resonances detected sharply are always TE modes.

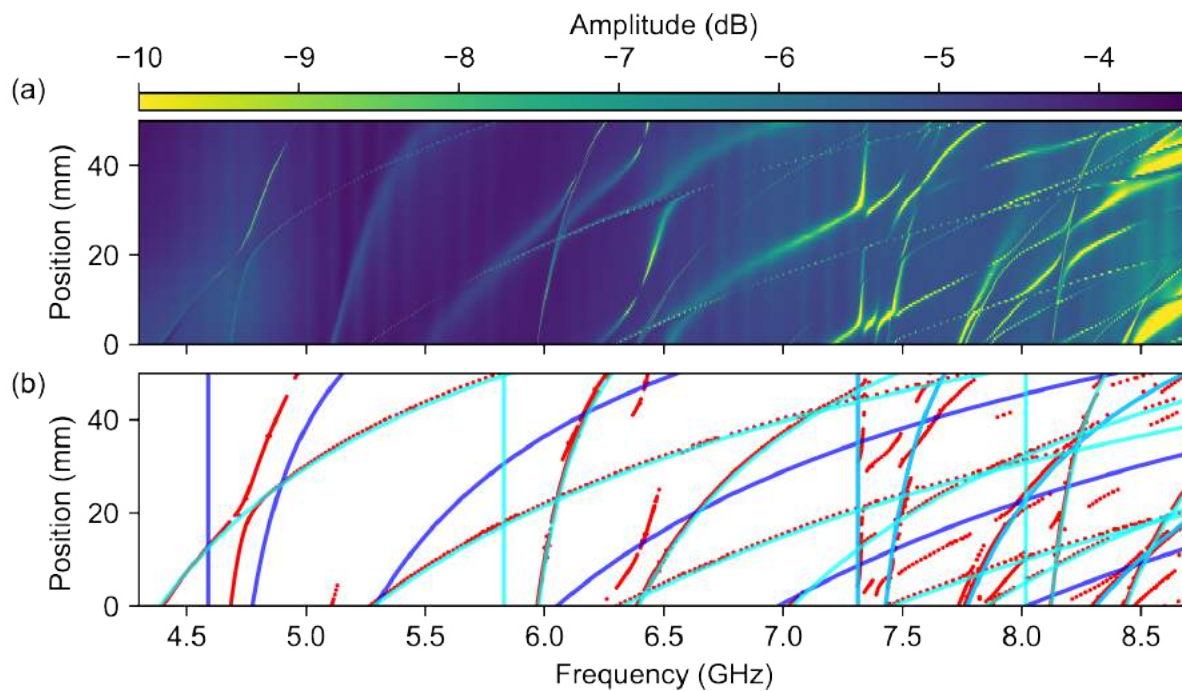


Figure 2.4 – **Characterisation and performance of the filter cavity** (a) Shows the Reflection, i.e.  $S_{11}(\omega)$  response of the filter cavity as the length of the cavity is changed. The resonances detected by our algorithm are shown as red dots() in (b) and we compare these with the theoretical dependence of the mode frequencies on the length where dark blue lines indicate TM mode and light blue lines indicate TE mode.

Next, we use the algorithm for detecting resonances, as described in the previous paragraph, and apply it to this data and the results are shown in the figure 2.4(b). We can also compare this result with the length dependence of resonant frequencies given by equation 2.1 and we can see in figure 2.4(b) that our results match quite well with the theory, and most of the resonances detected sharply are always TE modes. This can be attributed to the fact that our antenna, being an open circuit, creates a large voltage and couples strongly into the TE mode. Whereas since the circuit is not closed, we do not have a strong flow of current and therefore weak coupling into the TM modes.



The first step for automatising this task is to find a way to detect the resonances within any trace obtained from a VNA. From the input-output theory for a coupling between a wave-guide and a resonator, we know that the phase response of the cavity around one of its resonant modes shows a sigmoidal curve in the frequency space. If we take a derivative of this sigmoid, we will see a sharp peak in the slope of the curve at the resonance frequency. We use this fact to detect if there are any resonant modes in a certain range of frequencies.

## 2.6 Brute force algorithm for Tuning

It can be noticed from the nature of the Figure 2.4(a) that there are many possible positions at which a resonant mode crosses a particular frequency. At some frequencies there are mode crossings and some resonant modes are too undercoupled that a desired level of noise filtering cannot be achieved. Due to these reasons, we manually select which resonant mode is ideal for fitting for different frequency ranges and make a "Lookup table", so that given a frequency, the table outputs a value of length of the filter cavity corresponding to the resonant mode that should be fit to this frequency. The Zaber motor then sets the length and we obtain a resonant mode in the vicinity of our desired frequency, in the frequency domain. Then we use a fine tuning algorithm to set the modes with a greater accuracy to the frequency we desire.

The fine tuning algorithm involves both motors of the system and turns them in an iterative fashion. We run the Zaber linear motor in a simple proportional feedback in order to minimize the error between the desired frequency and the point corresponding to the minimum depth within the span of the VNA, which is usually set to 100 MHz. The algorithm for changing the external coupling of the filter cavity works in similar fashion. We first scan the angular position of antenna by  $2\pi$  radians so that it covers all the possible positions and note the maximum depth attained at each position. Next, we set the motor roughly back to the position which gave us the maximum depth. This does not work perfectly as there is some non-rigidity in the antenna so that it may not perfectly come back to the position that resulted in the maximum extinction previously. Due to this we need to run a further feedback loop that measures the depth, turns the motor in one direction by a predefined step, keeps going in the same direction if the depth has increased and turns in the other direction, while reducing the step size if the depth has decreased.

### 2.6.1 Tunability with the brute force algorithm

For the application mentioned in the section 2.3, we need to be able to tune the resonances of the filter cavity to multiple desired frequencies in a relatively small range of 1-10 MHz. The algorithm described in the previous section 2.6 was tested to check if it suffices for this purpose at example frequencies around 6.4 GHz.

Another test of the system + algorithm would be how accurately it can tune to a frequency. To obtain statistical data on the tunability, the algorithm was run over 1000 iterations to tune the filter cavity between two frequencies 5.125 GHz and 5.130 GHz. After the algorithm terminates, we take the complex scattering data from the VNA and use the circlefit algorithm [22] to estimate the resonance frequency and the external coupling rate of the fitted resonances. We then plot a histogram in frequency to see how well our algorithm performed. Figure 2.6 shows the resulting histograms.

We estimate the mean and standard deviation of all the fitted resonances, which is also shown in the plot. The mean is less than 2 kHz away from the desired frequency, which represents the maximum possible accuracy of the system and twice the value of the standard deviation represents the precision with which the system can be tuned. The accuracy and precision of the system are dependent on the minimum step size of the Zaber Linear stage motor as well as the mechanism that connects the motor to the piston of the filter cavity. It was observed that the motor, when it is moved by a very small amount, cannot exert sufficient force on the piston to overcome the static friction between the piston and the walls of the cavity. To overcome this issue, we sprayed the walls of the piston with a Teflon spray, to reduce this friction. The results in the figure 2.6 are after the addition of the Teflon spray. It should also be noted that the

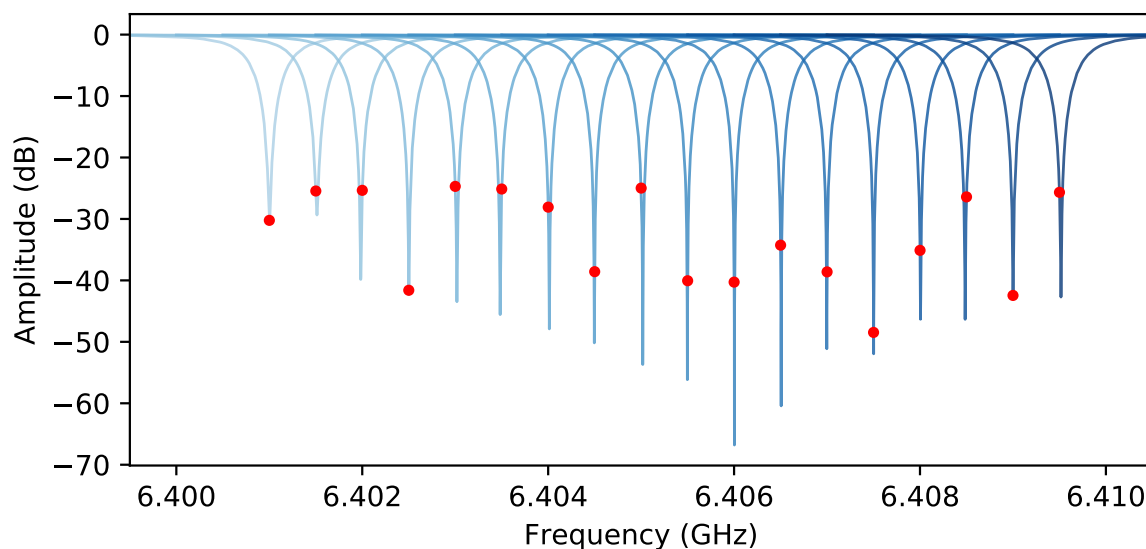


Figure 2.5 – **Fine tunability of the system:** By using the brute force algorithm, the filter cavity system was tuned to multiple frequencies in the range of 10 MHz, in the steps of 0.5 MHz. Shades of blue are used to distinguish between each individual traces of the VNA response of the system  $S_{21}$

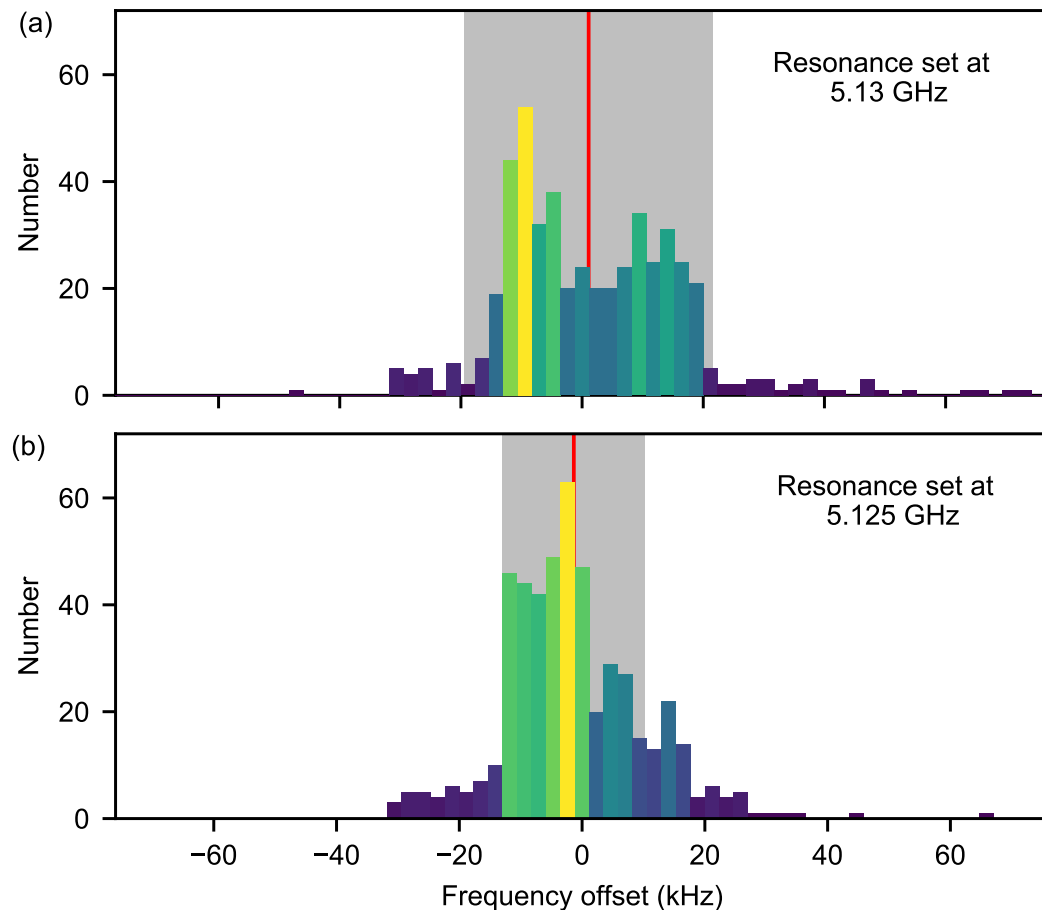


Figure 2.6 – **Accuracy and Precision of the tuning:** The filter cavity was repeatedly tuned to two frequencies by running the algorithm, and after each instance of the program running, the resonance frequency was estimated. This figure shows the histogram of the estimated frequencies at (a) 5.125 GHz and (b) 5.130 GHz. The black line indicates the mean of the histogram and the grey area represents the standard deviation.

histogram in Figure 2.6 (a) appears to be somewhat bimodal as compared to Figure 2.6 (b). This reflects the fact that the motor can only move in finite steps and not continuously.

## 2.7 Filtering the phase noise

Next we use an Spectrum analyser to measure the phases noise of our system. Instead of simply measuring in the system in reflection ( $S_{11}$ ), we now add a circulator to the filter cavity and measure transmission, so that we can send in a microwave signal and then estimate how the

filter cavity modifies it. We use the microwave source Keysight N5183B, we can quantify the phase noise of this source using the spectrum analyser (R&S FSW26).

We send a microwave signal at  $\omega_L = 2\pi \times 6.4$  GHz and Figure 2.7 shows phase noise up to 10 MHz away from this signal. We run the algorithm to tune the filter cavity at different detunings starting from 1 MHz in the steps of 0.5 MHz. The resulting spectrum of noise power is shown in the 2.7 and we can see that as much as 10 dB of extinction can be achieved in the phase noise spectrum at the desired frequency.

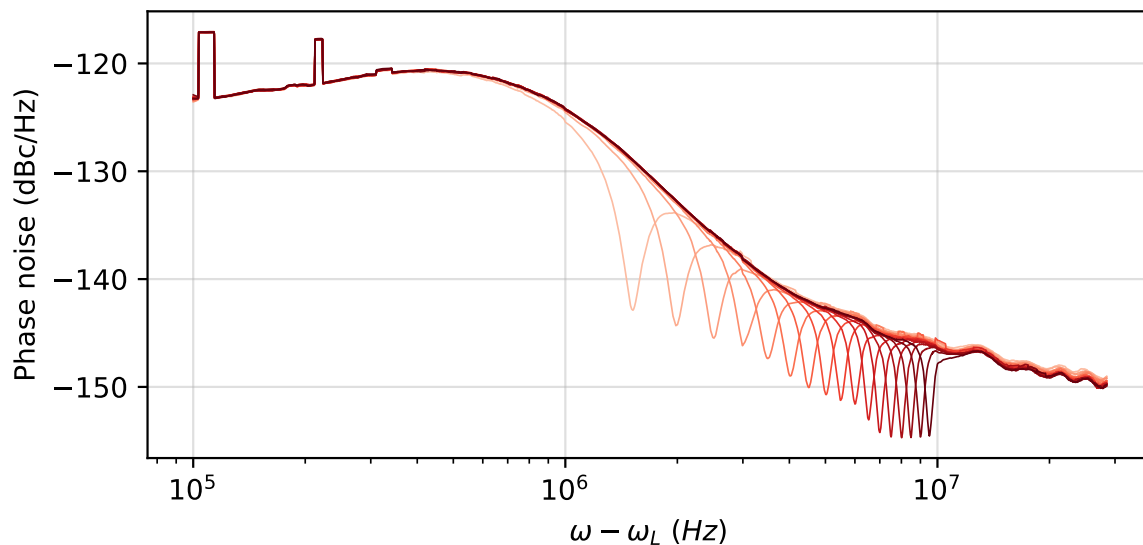


Figure 2.7 – **Phase noise filtering** A microwave tone was sent to the filter cavity at  $\omega_L = 6.4$  GHz and while running the same scan as 2.5, the phase noise around the tone was also measured.

## 2.8 Failure of the brute force algorithm

There are several cases when the algorithm fails to give us an accurate result -

Whenever there are two resonances in the VNA trace around the desired frequency where the filter cavity is to be tuned, our algorithm fails. This is because it cannot distinguish between the two resonances and at every iteration chooses to fit one which is deeper at the moment. Which results in the two resonances being chosen randomly and hence the algorithm does not converge.

The second reason is that even in the cases that the algorithm converges, it does not necessarily converge to the minimum that we want. The reason behind this can be considered from a graphical representation. If we consider the parameter space of the two independent parameters- the length of the cavity and angular position of the antenna, and plot a function that returns the depth at the frequency of interest, we get the following plot-

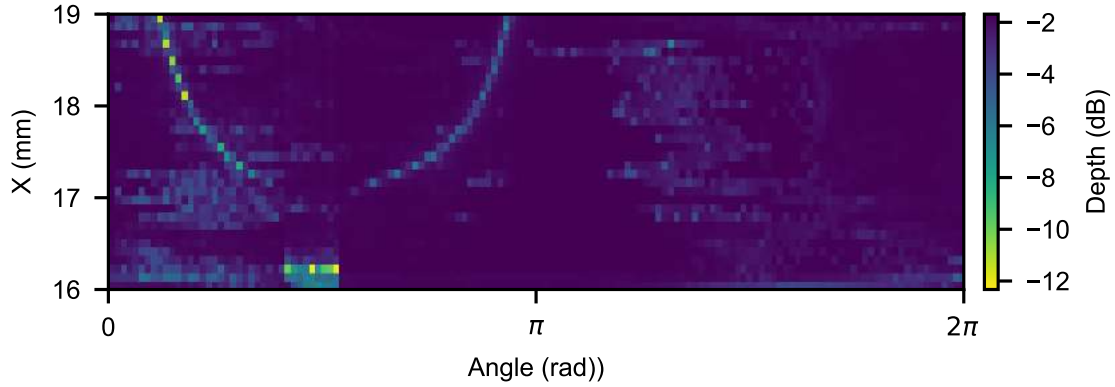


Figure 2.8 – **Parameter space:** Figure shows the extinction of the microwave signal sent at the frequency of interest.

We can see that in this parameter space, our algorithm always moves along one of the two parameter axes as we always tune the two parameters one after the other, for 3 iterations. However, this is not at all an efficient or mathematically rigorous way of finding a minimum of a function and it does not guarantee that the minimum will be reached. Not only that but even the function that we want to minimize is not a smooth function but has very sharp localised peaks.

To solve these two issues, we define a new “Cost function” that we are interested in minimizing-

$$C(\omega_k, D) = \left( \frac{\omega_k - \omega}{E_\omega} \right)^2 + \left( \frac{D}{E_D} \right)^2 \quad (2.2)$$

where,  $\omega$  is the frequency of interest to which we want to tune the filter cavity,  $\omega_k$  is the frequency of the resonant mode detected by the peak detection algorithm in the vicinity of  $\omega$ , and  $D$  is the depth of this resonance in the amplitude of the scattering parameter, in linear scale and not our usual dB units.  $E_\omega$  is the minimum value of the error in the frequency that we want to achieve, and  $E_D$  is the minimum value of the depth that we want to achieve. The values taken in implementation are  $E_\omega = 2\pi \times 10$  kHz and  $E_D = 10^{-3}$  or 30 dB in the logarithmic scale.

Defining the cost function in such a way ensures that it is smooth and has a non zero value of gradient over a large range in parameter space so that our minimisation algorithm can smoothly descend down this hill, as opposed to looking for a small pit in a large field, which was the case in the previous implementation.

(Note: I had intended to make a plot of the newly defined cost function similar to the figure 2.8, but I could not take this measurement as the lab was closed due to the coronavirus epidemic)

## 2.9 Nelder-Mead algorithm

There are many optimisation algorithms available in the literature for minimizing a function. We need to focus our attention on ‘gradient free’ algorithms as it is not possible to change the parameters by extremely small amount and estimate the derivative of the function, so we have to rely only on evaluating the cost function.

One such algorithm is the Nelder-Mead algorithm, named after its creators. This algorithm proceeds by starting out with a ‘simplex’, i.e. a set of points, of size  $N + 1$ , where  $N$  is the number of dimensions of the parameter space (2 in our case). It evaluates the function at all  $N + 1$  points and calculates the centroid of all these points. Then, it changes the point for which the function is maximum to a new point, depending on calculated according to a series of conditional reflection, expansion, contraction and shrinking of the polygon formed by the simplex. More details on this algorithm can be found in [23, 24].

The Nelder-Mead algorithm is implemented in the SciPy library’s `Optimize.minimize` function. We use this implementation to minimize the cost function defined in Equation 2.2. For every iteration of the algorithm, the cost function is evaluated several times, by taking the trace of the VNA, and using the peak finding algorithm to get the resonance frequencies of the modes  $\omega_k$  in the vicinity of  $\omega_0$ . The depth is taken simply as a difference of the deepest point from the average of the response in the region of frequencies where there is no resonance. For the initial simplex, the three points in parameter space are chosen in the following way- we first use the lookup table to set the resonance in the vicinity ( $\sim 200$  MHz) in the  $\omega_0$ , This gives us one value of position of the linear motor. Then we start scanning the angular position of the antenna, and stop when we get a depth of a resonance to be equal to  $-25$  dB. We thus obtain a point  $(x_1, \phi_1)$ , and then we can obtain other two points by moving along to parameters once independently, i.e.  $(x_2, \phi_2) = (x_1 + 1mm, \phi_1)$  and  $(x_3, \phi_3) = (x_1, \phi_1 + 30^\circ)$ .

### 2.9.1 Tunability with the nelder mead algorithm

Figure 2.9 illustrates the performance of our algorithm over coarse tuning. The filter cavity system was tuned to the frequencies in the range of 4.5-8.5 GHz in steps of 250 MHz. It can be seen that the algorithm can successfully tune to the depth of  $>20$  dB.

In contrast, we are also interested in investigating the performance of the algorithm over fine tuning. The filter cavity system was tuned to multiple frequencies in the range of 20 MHz, in the steps of 0.5 MHz. It can be seen that the algorithm can successfully tune to the depth of  $>20$  dB.

To check if the algorithm is successful, we repeat the measurement in the figure 2.9, over 20 iterations to see how robust our algorithm is.

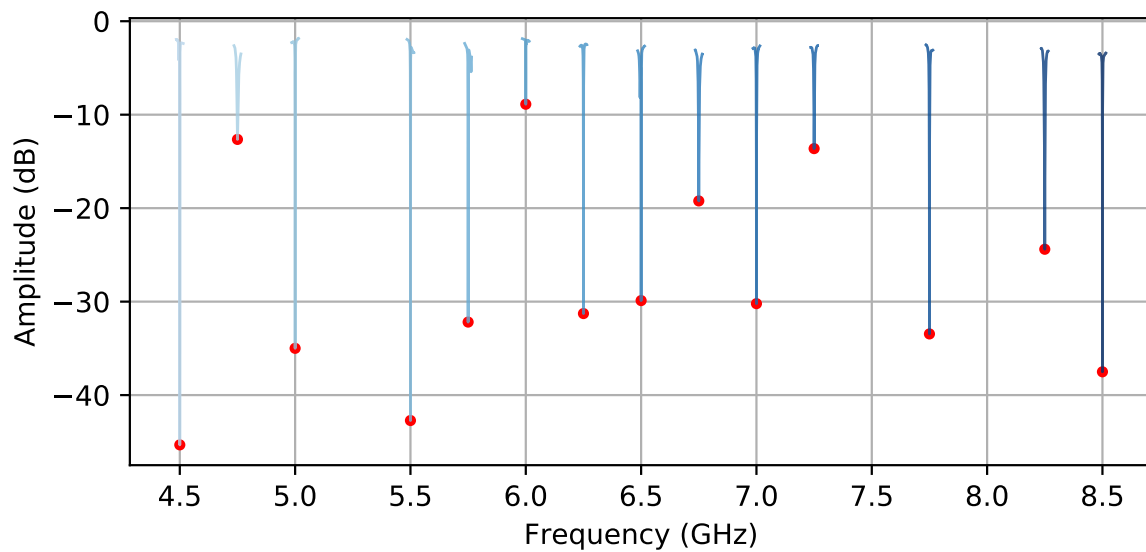


Figure 2.9 – **Coarse tunability of the system with Nelder-Mead algorithm** Shades of blue are used to distinguish between each individual traces of the VNA response of the system  $S_{21}$ . Red dots indicate the depth at the desired frequency

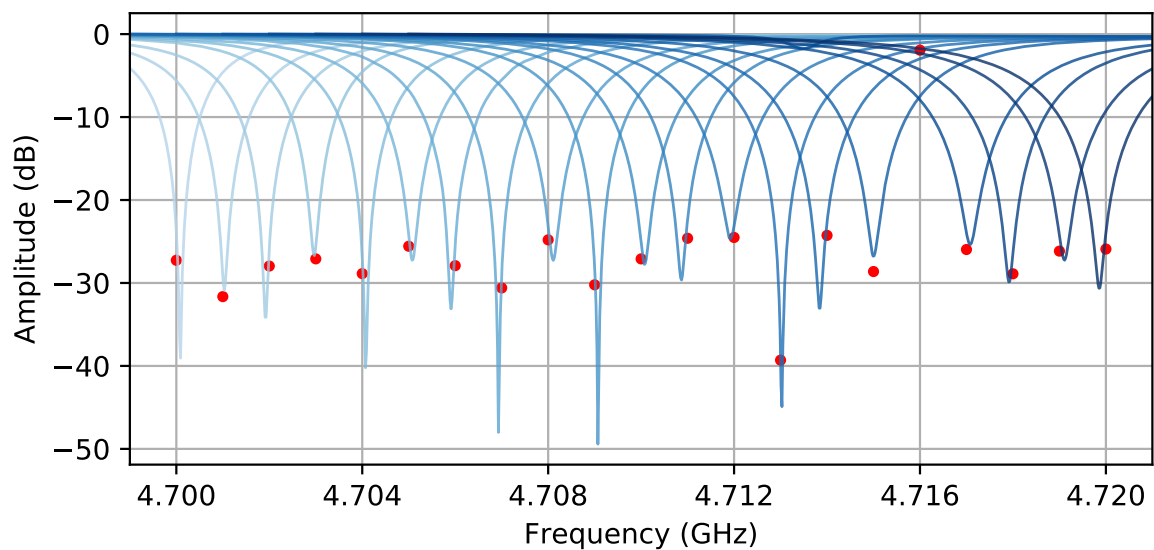


Figure 2.10 – **Fine tunability of the system with Nelder-Mead algorithm** Shades of blue are used to distinguish between each individual traces of the VNA response of the system  $S_{21}$ . Red dots indicate the depth at the desired frequency.

## 2.9.2 Benchmarking the Coarse tunability

In contrast to the extinction, which is of practical importance but has no physical meaning, we consider estimating the Q factor of the resonances in the figure 2.11. To find the Q factors, we

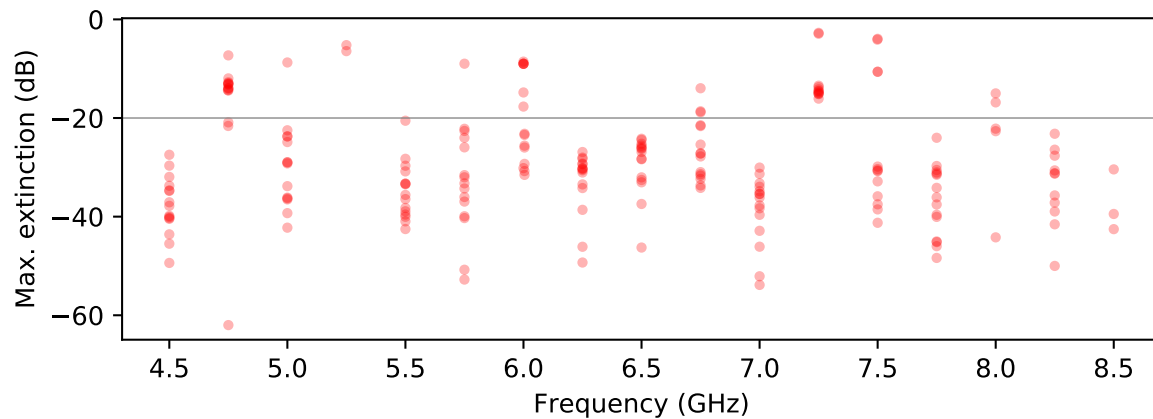


Figure 2.11 – **Coarse tunability of the system over 20 iterations** This plot shows the extinction achieved at the frequency of interest.

use the circlefit algorithm [22] to fit the cavity with the function given by the equation 1.2. This fitting procedure gives us the values of resonant frequencies ( $\omega_c$ ) and the cavity linewidth ( $\kappa$ ). Q factor can then be determined simply as the ratio-

$$Q = \frac{\omega_c}{\kappa} \quad (2.3)$$

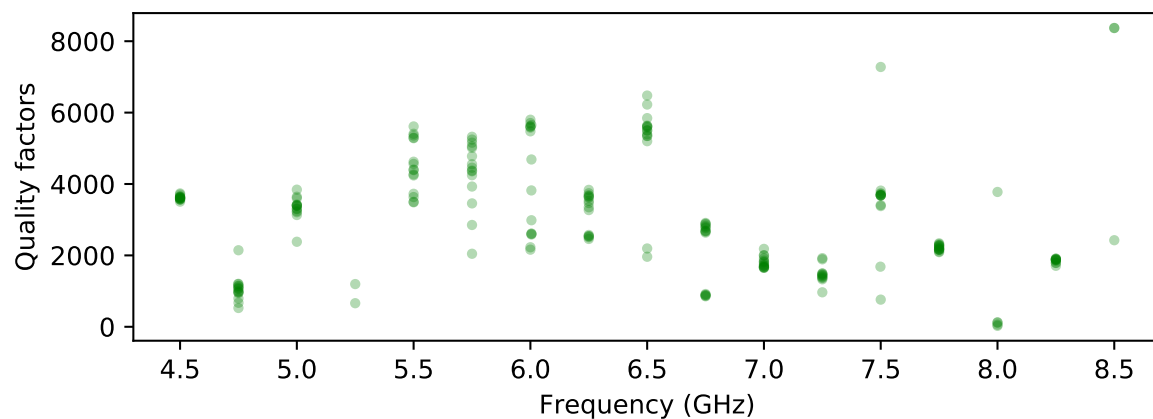


Figure 2.12 – **Q factors of the fitted resonances** Q factors of the various resonances tuned to the frequencies in the range of 4.5-8.5 GHz in steps of 250 MHz.

The values of the quality factor measured in our experiment can be compared to the filter cavities of [25]. We have achieved quality factors of the order of 2000-6000. It should be noted that the higher quality factors of [25] must be attributed to the fact that their filter cavities are kept at cryogenic temperatures that improve the loss.



## 2.10 Conclusion

To conclude, I was successfully able to write a program that can tune the frequency of the filter cavity with the precision and accuracy of 50 kHz in wide range of frequencies from 4.5 GHz to 8.5 GHz. This instrument will be useful in the future experiments such as optomechanical ponderomotive squeezing of microwaves, as well as experiments with superconducting qubits.

# 3 Optical readout of cryogenic superconducting systems <sup>I</sup>

In this chapter, I will outline the experiment carried out in the lab to measure signals from a superconducting electromechanical device, by converting the microwave signal to the optical domain using a LiNbO<sub>3</sub> electro-optic phase modulator kept at the temperature of 3 K inside a cryogenic dilution refrigerator. My contributions to the experiment in terms of characterisation of the phase modulator as well as an amplitude modulator at low temperature are highlighted.

## 3.1 Lithium-Niobate modulators

The second order nonlinear optical susceptibility  $\chi^{(2)}$  of the LiNbO<sub>3</sub> crystal gives rise to the linear electro-optic effect, where the refractive index of the crystal is modified depending to the applied electric field. [26]

The refractive index for the light wave travelling in a certain direction is given by taking a cross section of the index ellipsoid defined by the displacement vector. The different points on the ellipse thus obtained correspond to the refractive index for a particular polarization. On the application of an electric field, this index ellipsoid is modified depending on the electro-optic coefficient tensor  $r_{ij}$ . As LiNbO<sub>3</sub> is anisotropic, it has well defined crystal axes. The largest component of this tensor is  $r_{33}$ , and thus, an arrangement in which the light will propagate along y-axis of the crystal and the applied electric field is along the z-axis is desirable for the most efficient modulation of the signal. The modulators can be x-cut or z-cut, where cut defines the crystal direction perpendicular to the surface on which electrodes are placed.

The half wave voltage, or  $V_\pi$  is defined as the voltage that induces a phase shift of  $\pi$ . It is

---

<sup>I</sup>Note: Contents of this chapter have been submitted for publication titled, “Cryogenic electro-optic interconnect for superconducting devices”, Youssefi A., Shomroni I., Joshi Y.J., Bernier N.R., Uhrich P., Lukaschuk A., Qiu L., and Kippenberg T.J.

given by the following relation-

$$V_{\pi} = \frac{d}{L} \frac{\lambda}{2r_{33}n^3\Gamma}$$

where  $d$  is the electrode gap,  $L$  is the total length of the electrodes along the waveguide,  $\lambda$  is the wavelength of the optical carrier,  $r_{33}$  is the electro-optic coefficient of Lithium Niobate along the direction,  $n$  is the ordinary refractive index of the Ti doped waveguide, and  $\Gamma$  is the overlap integral for the electrical and optical fields. The formula makes intuitive sense in following ways- shorter the electrode gap, higher will be the electric field and it will modulate the refractive index strongly; Longer the distance over which the phase shift is induced, shorter the potential required to obtain the same phase shift and so on.

The lithium niobate electro-optic modulators can be of two types- a phase modulator or an amplitude modulator. Consider an optical signal  $Ae^{i\omega t}$ . A phase modulator has a single optical waveguide and a phase of  $e^{i\phi}$  is imparted to the optical signal to give  $Ae^{i\omega t+i\phi}$ , where the phase depends on the applied electric voltage as-  $\phi = \pi \frac{V}{V_{\pi}}$ . An amplitude modulator is essentially a combination of two phase modulators, where the incoming optical signal is split into two paths and one is imparted a phase change of  $e^{i\phi}$  and the other a phase change of  $e^{-i\phi}$ . When the two paths are recombined, we get the resulting optical signal to be  $= Ae^{i\omega t}(e^{i\phi} + e^{-i\phi}) = \frac{A}{2} \cos(\phi)e^{i\omega t}$ . As the amplitude modulation results from interfering the two signals, this design is also termed as ‘Mach-Zehnder modulator’ after the famous experiment.

Previous experiments have investigated the temperature dependence of the electro-optic coefficient and the refractive index of  $\text{LiNbO}_3$  [27], and show that the value of  $r_{33}$  decreases on cooling. Commercial LN modulators were also tested in the cryogenic environment in Ref [28] and [29]. The  $V_{\pi}$  of x-cut modulators was measured down to temperatures of 10K and it was shown to increase by 12% from its value at room temperature. Authors of Ref [30] discuss behaviour of LN modulators with superconducting electrodes down to 4K and report a slight increase in  $V_{\pi}$  on cooling. However, no such devices have been tested in a cryogenic environment to readout a superconducting system. This was the main focus of the project being carried out in the lab. However, it was also necessary to repeat the measurement of the  $V_{\pi}$  and make sure that we obtain the similar results as obtained previously.

## 3.2 Experimental setup

Figure 3.1 shows the complete schematic of our experimental setup. Signals generated by a Keysight N5183B signal generator are sent to the device under test via microwave coaxial lines embedded with cold attenuator. The reflected signal from the electromechanical device is split into two. One signal is detected via the conventional measurement chain with the HEMT and

room temperature amplifiers. The second signal is sent to the EO phase modulator kept at the 3 K flange of the dilution refrigerator. The optical fibers from the fridge are connected to the optical fibers outside the fridge via vacuum compatible optical feedthroughs.

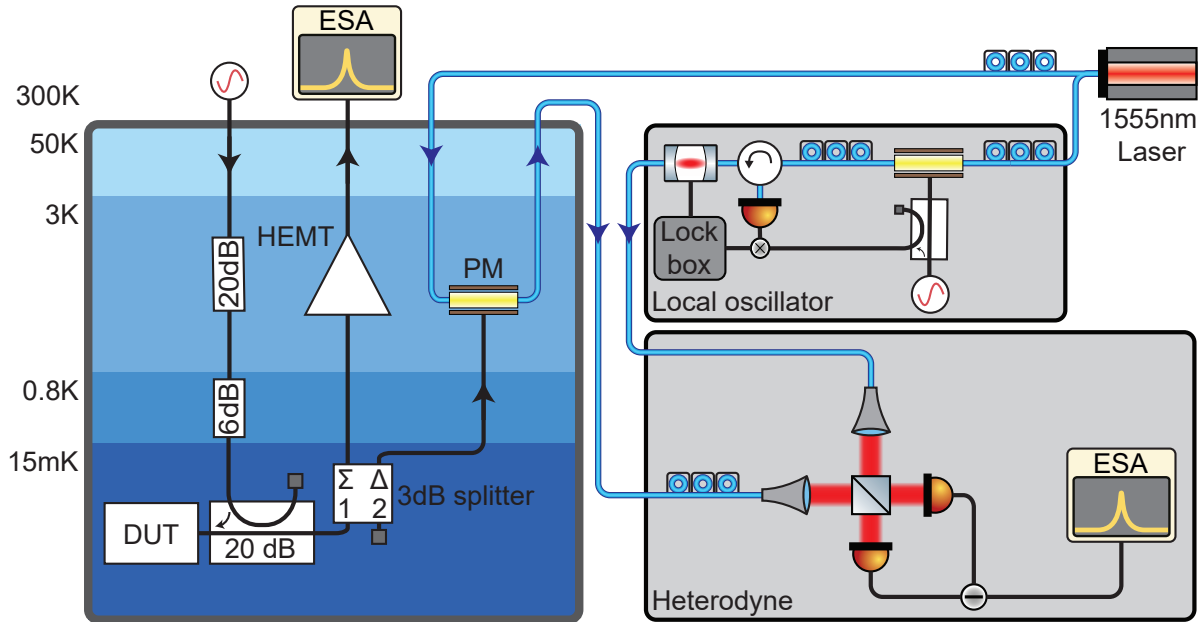


Figure 3.1 – **Electro-optic readout of a superconducting electromechanical system** Experimental scheme to measure the superconducting scheme

### 3.2.1 Heterodyne detection

Next we need to detect this signal which has peaks at frequencies of  $\omega_L$ ,  $\omega_L + \Omega$ , and  $\omega_L - \Omega$  in its power spectral density. However, photodiodes can measure signals fluctuating at such high optical frequencies. Therefore we need to mix down our signal to low frequencies. For this purpose, we interfere our signal with a local oscillator of frequency  $\omega_L + \frac{\Omega}{2} + \delta$ . This gives us two beat signals- between the laser tone and the local oscillator of frequency  $\frac{\Omega}{2} + \delta$  and between the phase modulated sideband and the local oscillator of frequency  $\frac{\Omega}{2} - \delta$ . These beat signals are detected by a single photodetector for the case of  $V_\pi$  measurement and a pair of balanced photodetectors for the case of optical readout experiments where an improved SNR is desirable.

### 3.2.2 Pound-Drever-Hall frequency locking

In order to generate the local oscillator at a frequency of  $\omega_L + \frac{\Omega}{2} + \delta$ , which in our case is about  $\sim 2.5$  GHz away from the laser frequency, we need to modulate the laser light so that it generates sidebands. For this purpose we again use a electro-optic phase modulator, Ixblue

MPZ-LN-10, and drive it with a microwave tone of the frequency  $\frac{\Omega}{2} + \delta$ . The phase modulator generates the sidebands of the laser and we consider the power spectral density of this signal after passing through the modulator, we will see peaks at the frequencies  $\omega_L$ ,  $\omega_L + \frac{\Omega}{2} + \delta$ , and  $\omega_L - \frac{\Omega}{2} - \delta$ . However, in the local oscillator we only want a signal at the frequency of  $\omega_L + \frac{\Omega}{2} + \delta$ , so for this reason we need to eliminate other two peaks from the signal. Hence we use an optical piezo-electric filter cavity (Micron Optics FFP-TF2 Tunable Filter), which we measure in transmission so that when the length of the filter cavity matches the optical sideband of interest, we get maximum transmission of power and other signals destructively interfere inside the cavity. However, this signal is not stable. Due to thermal and mechanical fluctuations, the length of the filter cavity is never constant and can easily change by small amounts of the order of few linewidths. To stabilize this system so that we get a constant amplitude local oscillator, we use following scheme termed the ‘‘Pound-Drever-Hall’’ frequency locking [31].

The optical filter cavity has a BNC input so that the piezo inside can change the length of the filter cavity according to the voltage that is applied. If we now have a way to detect exactly the natural fluctuations of the cavity then we can appropriately apply the right voltage so as to cancel these fluctuations precisely. For this purpose, we detect the reflected signal with a photodiode and we feed it to a lockbox (New Focus LB1005 Servo controller) to generate an error signal. As has been established previously, the amplitude dip of an optical cavity is symmetric around resonance. Hence to know whether the frequency fluctuation of the laser is above or below the cavity frequency, we need to measure the phase of the reflected signal. This is done effectively by generating upper and lower sidebands of the laser beam using a phase modulator, as has been described before and the error signal can be generated by the interference of the sidebands with the carrier. In standard PDH scheme, we lock our laser signal to maintain the error signal at the carrier frequency to zero, but in this case, since we want our local oscillator to be at the upper sideband, we lock to this upper sideband. This gives us a stable local oscillator at the frequency  $\omega_L + \frac{\Omega}{2} + \delta$ .

### 3.3 Measurement of half-wave voltage

Consider an optical signal, coming from a laser of the frequency  $\omega_L$ . In our case, we use a NKT Kohreas laser, of the wavelength 1550 nm. The signal of the laser can be described as a classical wave of a constant amplitude-

$$E(t) = Ae^{i\omega_L t}$$

This signal is sent through an electro-optical phase modulator (EOM), in our case a commercial Thorlabs LN65-10-S-A-A-BNL, of 10 GHz microwave bandwidth. We send a microwave tone

of the frequency  $\Omega$  to the microwave port of the EOM, in our case using a microwave source Keysight N5183B and at  $\omega = 5\text{GHz}$ . This can be described by the The refractive index of the material and therefore the phase of the signal is modulated according to this microwave signal in the following manner-

$$E(t) = Ae^{i\omega_L t + \frac{i\pi}{V_\pi} V(t)} = E_0(t) e^{\frac{i\pi}{V_\pi} V(t)}$$

Where  $V(t)$  is the applied microwave voltage on the electrodes of the EOM and  $\frac{\pi}{V_\pi}$  denotes the modulation depth. Let us consider that we are driving the EOM with a microwave tone of frequency  $\Omega$ . We consider  $V(t) = V_0 \cos(\Omega t)$

$$E(t) = E_0(t) e^{i\frac{\pi}{V_\pi} V(t)} \approx E_0(t) \left( 1 + \frac{i\pi V_0}{2V_\pi} (e^{i\Omega t} + e^{-i\Omega t}) \right)$$

Where we have assumed the drive voltage amplitude ( $V_0$ ) to be much smaller than the half-wave voltage. This is justified as the power in the signal coming from the superconducting devices is usually several orders of magnitude lower than the  $V_\pi$  of the EOMs. The simplified equation shows that the EOM creates two phase modulated sidebands, which are equal to one microwave drive tone frequency away from the laser carrier frequency, and the ratio of their amplitude to the amplitude of the carrier, the so called ‘modulation depth’ can be given by-

$$\beta = \left( \frac{\pi V_0}{2V_\pi} \right)^2 \quad (3.1)$$

We can measure the modulation depth  $\beta$ , and from that we can infer the  $V_\pi$  of the system using the following formula-

$$V_\pi = \frac{\pi}{2} \sqrt{\frac{2ZP_\Omega}{\beta}} \quad (3.2)$$

where,  $Z$  denotes the characteristic impedance of the microwave circuit, which in our case is equal to 50 Ohms. It should be mentioned that this is due to the fact that the manufacturer of the EOM has added a 50 Ohm termination at the end of the microwave circuit of the EOM.  $P_\Omega$  denotes the power of the microwave signal at the EOM.

### 3.3.1 Calibration of Microwave power reaching the EOM

To measure the  $V_\pi$  of our system accurately, we also need to estimate the power of the microwave tone reaching the phase modulator inside the dilution refrigerator. It is slightly less than the power at the microwave source because the coaxial cables that go into the fridge have some

losses. To maintain generality, we assume that these losses are temperature and frequency dependent.

As a first step, the Insertion losses at the room temperature can be explicitly measured when the refrigerator is opened. Instead of connecting to the microwave source, we connect the input coaxial cable to the port-1 of the VNA. A sufficiently long coaxial "calibration" line is connected from port-2 of the VNA to the input coaxial cable at the EOM. Now we measure the  $S_{21}$  response of the input line + calibration line. Let us denote this frequency dependent attenuation by  $\alpha_1(\omega)$ , in the units of dB. Next the calibration line is connected between the two ports of the VNA and it gives us the attenuation  $\alpha_2(\omega)$ . Now, we can infer the attenuation of the input line to the EOM simply as-

$$\alpha_{input}(\omega) = \alpha_1(\omega) - \alpha_2(\omega)$$

where all values are in dB scale. Figure 3.2 (a) shows the attenuation of the input line thus inferred at the room temperature.

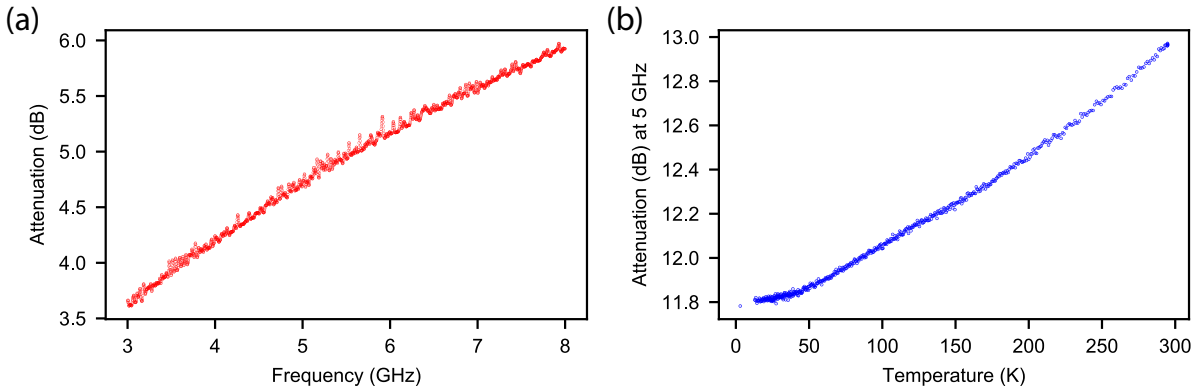


Figure 3.2 – (a) shows the insertion loss in the input line to the EOM as a function of frequency at room temperature. (b) shows the attenuation in the temperature calibration chain as a function of temperature at 5 GHz

Next we need to know how the attenuation in the coaxial cables depends on the temperature. For this purpose, we take two additional lines at the same 3 K stage of the dilution refrigerator that are identical to the input line that goes to the EOM. We connect these lines to each other at the 3 K stage and we connect the other two ends at the VNA so that we will effectively measure the attenuation of this ‘Temperature calibration chain’. We keep taking the VNA traces as we cool down the the refrigerator, so that we can know the temperature dependence of the the insertion losses in this line and from that we can infer how the attenuation of the input to the EOM changes with the temperature. Figure 3.2 (b) shows the attenuation of the temperature calibration chain as the temperature of the 3 K stage goes from room temperature down to 3 K.

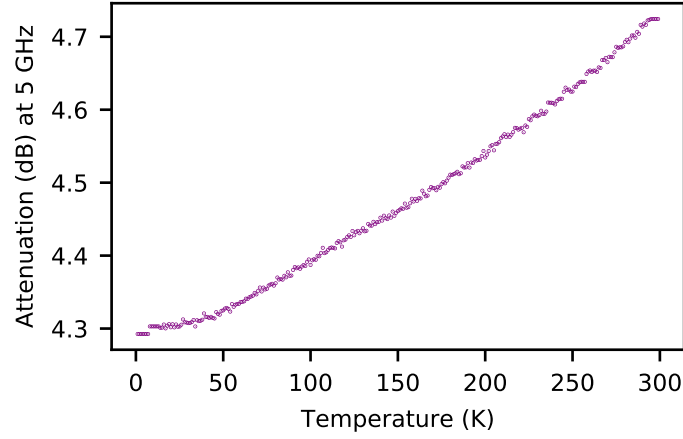


Figure 3.3 – The insertion loss in the input line to the EOM at 3 K stage as a function of temperature

We can measure the percentage change in the insertion loss of two lines and we assume that the change in the insertion loss of the input line of the EOM changes exactly by this percentage. Quantitatively,

$$\alpha_{input}(T) = \alpha_{input}(T_{room}) \left( 1 + \frac{\alpha_{tc}(T) - \alpha_{tc}(T_{room})}{\alpha_{tc}(T_{room})} \right) \quad (3.3)$$

Where  $\alpha_{input}(T)$  denotes the insertion loss of the input line to the EOM at any arbitrary temperature ‘T’,  $T_{room}$  indicates the room temperature, and  $\alpha_{tc}$  indicates the insertion loss of the temperature calibration chain. Thus, the inferred attenuation in the input line is plotted in Figure 3.3-

And hence, we can accurately estimate the microwave power received by the EOM while doing the experiment to infer the  $V_{\pi}$  by measuring the modulation depth.

### 3.3.2 Temperature dependence of the half-wave voltage

We use the calibration data obtained in the figure to estimate the power reaching the phase modulator at 3 K stage. We measure the modulation depth  $\beta$  using the heterodyne detection scheme explained previously and also depicted schematically in the Figure 3.5 (a). Thus we now have all the variables needed to measure the  $V_{\pi}$  of the EOM. For each measurement, we measure the modulation depth at several powers and then perform linear regression to fit the modulation depth and power. The  $V_{\pi}$  is extracted from the slope of this line. We repeat this measurement over and over again, starting from room temperature and we cool down our dilution refrigerator



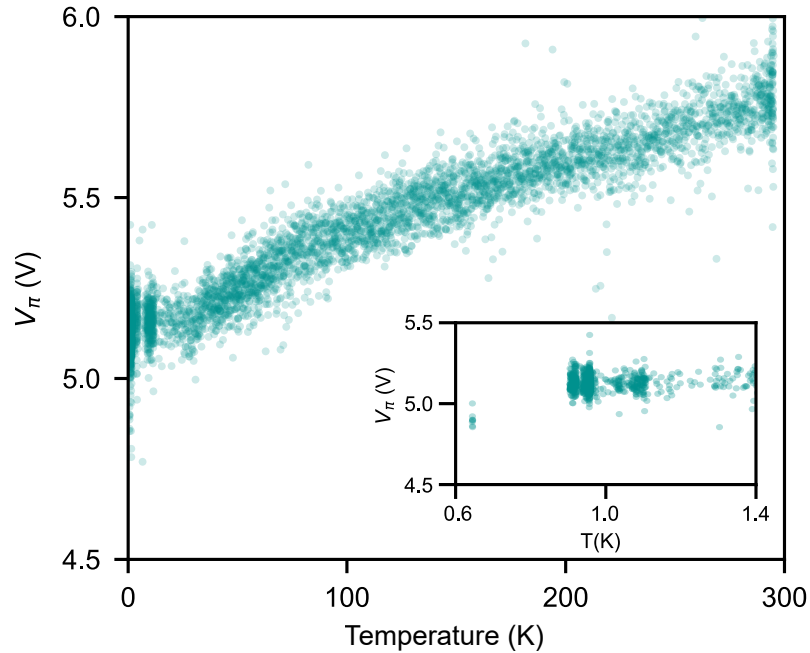


Figure 3.4 – Continuous measurement of  $V_{\pi}$  as the temperature is lowered. The inset shows the data around 1 K. The minimum temperature at which the  $V_{\pi}$  is around 600 mK

to its base temperature. Since for this measurement, we mount the EOM at the so called 800 mK stage of the dilution refrigerator, whose temperature can indeed be lowered further til 600 mK by turning off the still heater responsible for keeping the temperature and the flow of Helium stable. Figure 3.4 shows the result of this measurement.

We can see that the  $V_{\pi}$  of the EOM decreases slightly with the temperature, i.e. we get improved performance. This result agrees with the previous reports [28–30] that the EOM survives and functions at the cryogenic temperatures and that the  $V_{\pi}$  does not change drastically, i.e. it is not affected by any phase transitions at the temperatures til 600 mK. However, a significant difference between the previous results and our result is that they show that the  $V_{\pi}$  increases as we decrease the temperature and in our case, it increases as we decrease the temperature. The increase is justified by the fact that the  $r_{33}$  decreases on decreasing the temperature. This apparent discrepancy remains unresolved.

### 3.3.3 Frequency dependence at cryogenic temperatures

Once we cool down our system to the minimum temperature of 600 mK, we change the frequency of the drive tone over the range of 3-8 GHz, which is usually the frequency range for electromechanical systems as well as superconducting qubits. Figure 3.5 (b) shows the low temperature dependence of the  $V_{\pi}$  on the frequency of drive tone.

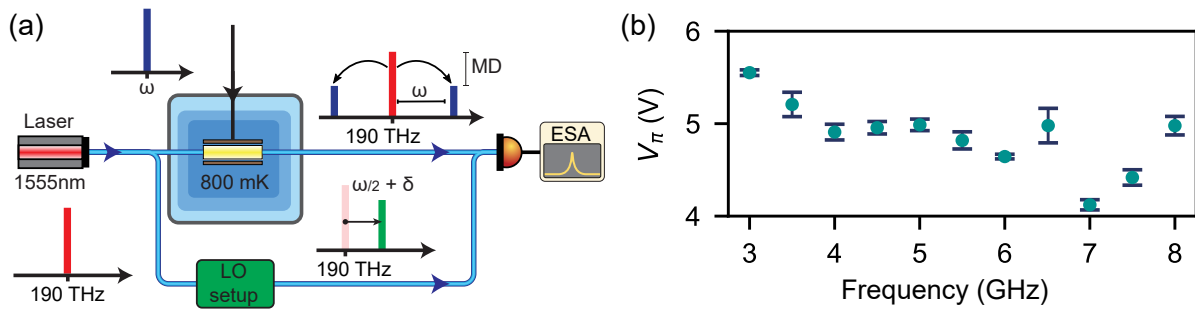


Figure 3.5 – (a) shows the scheme for measuring the  $V_\pi$  (b) shows the dependence of the  $V_\pi$  on frequency of the drive tone at cryogenic temperatures of 600 mK

### 3.4 Investigating heating due to Optical power dissipation

To assess the viability of using an electro-optic phase modulator at the 800mK stage of a dilution refrigerator, we need to make sure that the Optical power dissipated by the EOM due to the transmission loss does not cause significant heating of the system and thermalise at a unusually higher temperature. The optical input power sent to the EOM was increased over time and the resulting change in the temperature was observed, allowing a thermalisation period of 20 minutes.

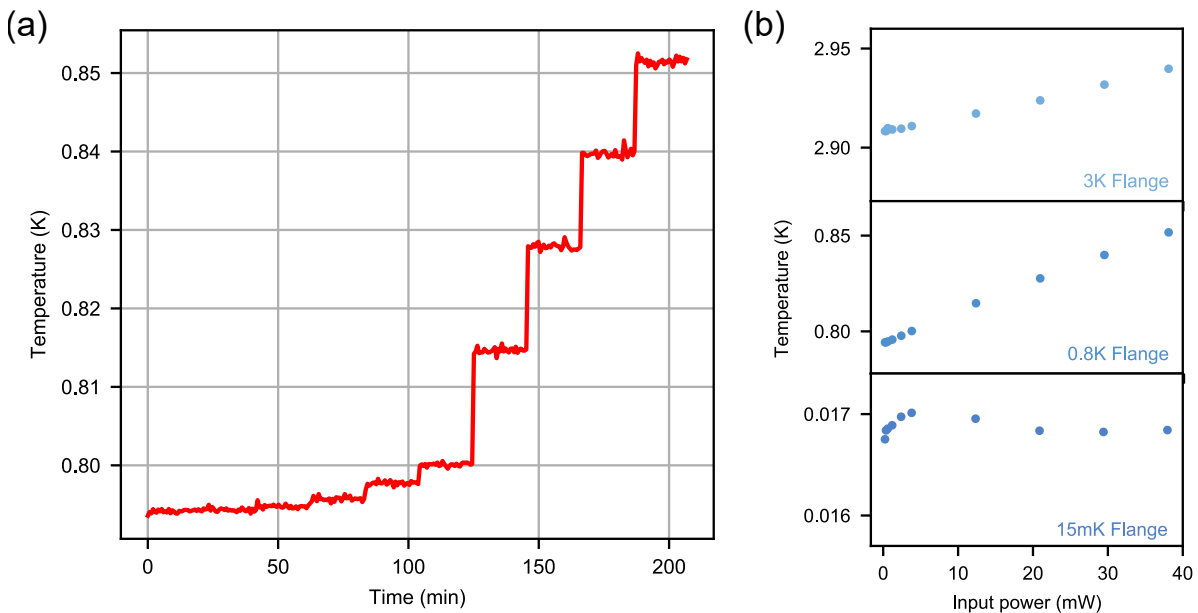


Figure 3.6 – (a) shows the time trace of temperature as power is changed in steps after every 20 minutes. (b) shows the thermalised temperature of the 3 K, 800 mK and 15 mK stages of the dilution refrigerator as the optical input power to the phase modulator kept at 800 mK stage is varied.

Figure 3.6 shows this effect due to optical heating. It can be seen that at the 800 mK stage, the dissipated optical power causes heating in the order of 10s of milikelvin and it increases linearly with the power. It is noteworthy that this does not cause any heating at the base of the refrigerator where the superconducting samples are kept. This is an important result that shows that, from an engineering point of view, the dilution refrigerator is compatible with the operation of phase modulators at the 800 mK stage. This implies, assuming that they each operate at 1mW input power, at least upto 40 phase modulators can be kept inside the fridge at the 800 mK stage and consequently 40 superconducting devices (for eg. qubits) can be optically read out.

### 3.5 Performance of an Amplitude moduator at cryogenic temperatures

As mentioned before, a Lithium niobate electro-optic modulators can either be a phase modulator or an amplitude modulator. We have already investigated the behaviour of the phase modulator. So now we would like to see what would be the effect of cooling down to cryogenic temperatures on an amplitude modulator.

An amplitude modulator also has an additional input called bias voltage. Because in a Mach-Zehnder geometry, the two optical path lengths cannot always be matched to the accuracy of the wavelength of the light, we might get constructive or destructive interference of the two waves depending on the phase difference in two paths. If we want ideal amplitude modulation,

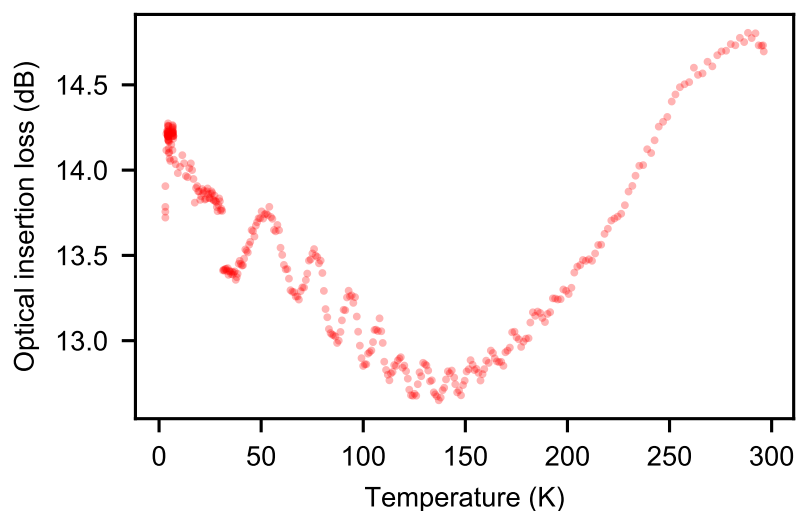


Figure 3.7 – The insertion loss of the amplitude modulator as it is cooled down to cryogenic temperatures.

this phase difference due to mismatch in path lengths should be made zero. For this purpose, an additional electrode is placed on one of the interferometer arms in order to change the phase of one path so that we can get rid of the phase mismatch. While conducting the experiment we need to change the bias voltage so that we get the maximum transmission of the optical signal.

We mount the amplitude modulator at the 3 K stage of the dilution refrigerator. After setting the correct bias voltage, we start cooling the dilution refrigerator and measure the transmission of the modulator as the temperature changes. Figure 3.7 shows the insertion loss, i.e. the ratio of output optical power to the input optical power, as a function of temperature.

The periodicity in the transmission is noteworthy. As explained before, the transmission is sensitive to the changes in optical path length. This periodicity can be explained by the fact that as we cool down the modulator, there must be some change in the optical path length due to thermal contraction.

### 3.5.1 Data transmission

Next, we also need to demonstrate that the amplitude modulator performs as expected. One standard way to demonstrate the operation of modulators, is a data transmission experiment. In such an experiment, data bits are sent to the modulator electronically. In case of the amplitude modulator, the amplitude of the optical wave is changed based on the incoming data bits. This experiment is easier with the amplitude modulator as compared to the phase modulator due to the simple fact that our photodetectors can directly detect the change in the optical amplitude but in order to detect the phase we need to do a homodyne measurement.

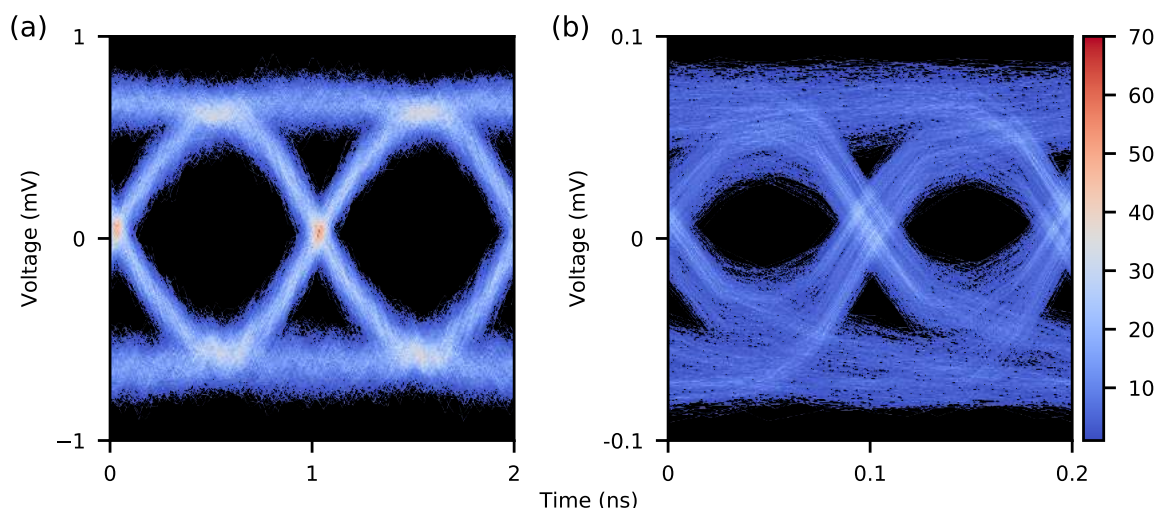


Figure 3.8 – The eye diagram resulting from the data transmission experiment at (a) Room temperature and (b) Cryogenic temperature.

To do this experiment, we use a Keysight M8195 arbitrary waveform generator, NRZ (non-return to zero) encoded bit stream at 1 GHz and 10 GHz to the amplitude modulator kept at 3 K stage in the dilution refrigerator. The optical signal from the amplitude modulator is simply detected by a Newport 1544-B photoreceiver. The signal from the photoreceiver is sampled with an oscilloscope Teledyne LeCroy MDA800, rated 40 GSa/s. Figure 3.8 shows the eye diagram thus observed for (a) 1 GHz signal at room temperature and (b) 10 GHz signal at cryogenic temperature. The fact that the “eye” is “open”, shows that the amplitude modulator is functional at the cryogenic temperatures and can be used to encode data in an optical signal which can be sent to long distances by means of an optical fiber.

### 3.6 Optical readout of optomechanically induced transparency

To demonstrate the electro-optical readout technique, we perform two tone spectroscopy and measure optomechanically induced transparency (OMIT) [32–34] on the electromechanical sample, by applying a tone on the lower motional sideband (red-detuned by  $\Omega_m$  from the cavity resonance) and sweep a second tone across resonance. The strong microwave pump cools the mechanical motion, resulting in a wider effective mechanical linewidth,  $\Gamma_{\text{eff}} = \Gamma_m + 4g^2/\kappa$ , while we observe this modified response by probing the cavity with an additional weak microwave probe. Because of the electromechanical coupling, the MW pump modifies the cavity response, resulting in a transparency window that appears on resonance of width  $\Gamma_{\text{eff}}$ . To compare the optical and HEMT readouts, the reflected signal is split and measured simultaneously using both techniques. In order to measure the coherent response via the electro-optical readout, we perform a heterodyne measurement with a frequency shifted local oscillator. The beatnote between optically transduced probe tone and the local oscillator generates a RF signal detectable with the photodetector.

The strong MW pump damps the mechanical motion, resulting in a wider effective mechanical linewidth,  $\Gamma_{\text{eff}} = \Gamma_m + 4g^2/\kappa$ . Because of the electromechanical coupling, the MW pump modifies the cavity response, resulting in a transparency window that appears on resonance of width  $\Gamma_{\text{eff}}$ . We observe this modified response by probing the cavity with an additional weak MW probe (Fig. 3.9). We performed the OMIT experiment for different pump powers and characterized the mechanical resonance frequency using the transparency feature. At high pump powers, when  $g \sim \kappa$ , we observe mode splitting as a result of strong coupling and mode-hybridization between the mechanical and microwave modes [35].

Figure 3.9f shows the OMIT results, with excellent agreement between the optical and HEMT readouts.

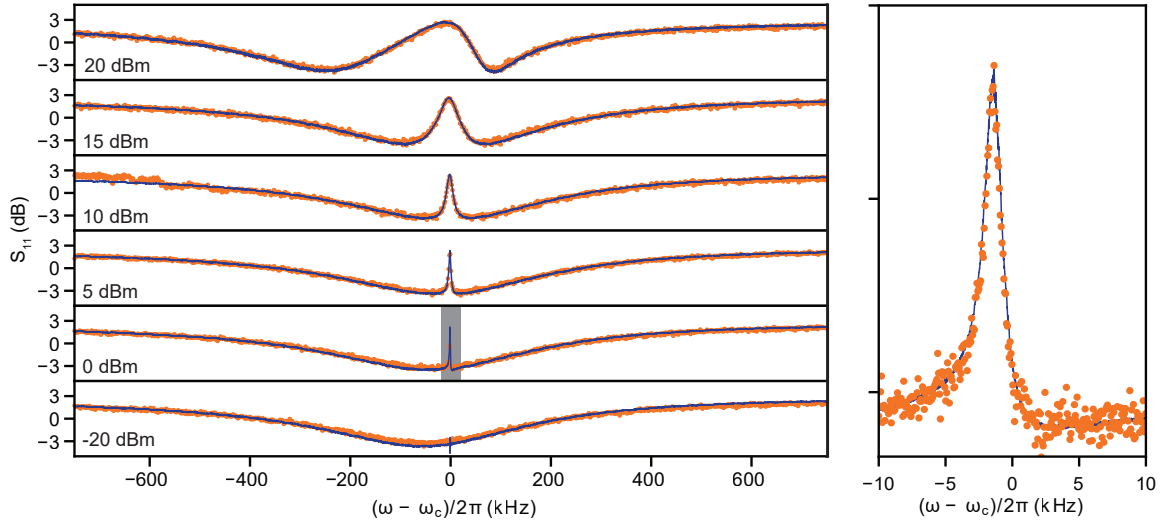


Figure 3.9 – Measurement of the electromechanical resonance for increasing MW pump powers of  $(-20, 0, 5, 10, 15, 20)$  dBm at the source, from bottom to top respectively. The probe power is  $-20$  dBm at the source. By increasing the pump power, optomechanical induced transparency window emerges and by pumping stronger modes get strongly couple leads to evaded crossing effect. Blue lines correspond to HEMT readout and orange dots to optical readout.

### 3.7 Observation of the parametric instability

We investigate incoherent signal detection using the optical readout and measure the power spectral density of a signal reflected by the electromechanical system. For this, we drive the mechanical oscillator into self-sustained oscillatory regime by pumping the system on its upper motional sideband,  $\omega_{\text{pump}} = \omega_c + \Omega_m$ , inducing a parametric instability [1, 36, 37]. Because the mechanical motion is amplified, correspondingly the optomechanical modulation of the input microwave tone is also amplified. The output microwave spectrum thus features strong sidebands around the microwave pump, at integer multiples of the mechanical frequency. Using our optical readout, we can detect these mechanical signals, and compare the results with the simultaneously-measured HEMT output (Fig. 3.10).

We first use the independently characterized added noise of the HEMT amplifier (referred to the input),  $n_{\text{add}}^{\text{HEMT}} \simeq 8 \text{ quanta}/(\text{s} \cdot \text{Hz})$ , to calibrate the power spectral density measured in the HEMT branch. Applying the same calculation to the optical readout, with the noise floor now consisting of optical shot noise, calibrates the optical output after the transduction.

We note that the frequency widening of the optically detected sidebands, observed in Fig. 3.10, is due to fluctuations in the LO frequency, caused by the limited bandwidth of the

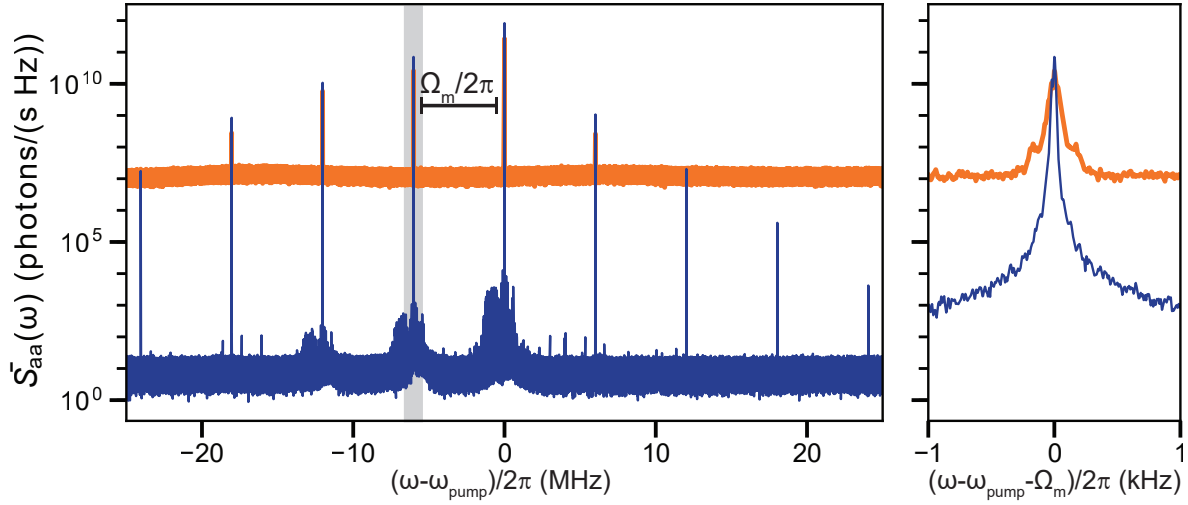


Figure 3.10 – Measured power spectral densities of the microwave pump (central peak) and mechanical sidebands detected by the HEMT (blue) and optical (orange) readouts. The right panel shows the power spectral densities of the on-resonance mechanical sideband highlighted with gray in the left panel.

locking setup in conjunction with using minimum possible resolution bandwidth,  $RBW = 1$  Hz in the spectrum measurement. The total sideband power, however, is conserved. Improving the LO locking setup or increasing the RBW in the optical measurement can reduce this effect.

### 3.8 Conclusion

Through this experiment, our team has been successfully able to demonstrate that the  $\text{LiNbO}_3$  phase modulators function at cryogenic temperatures, and that they can be used as interconnects to read out superconducting systems usually operating at the sub-Kelvin temperatures.

From the Figure 3.10, we can compare the signal to noise ratios of the HEMT and the EOM, and we find that the SNR for the EOM is 65 dB smaller than the SNR for the HEMT. The noise floor of the HEMT, as described before is at  $8 \text{ quanta}/(\text{s} \cdot \text{Hz})$ , which is equal to  $-195 \text{ dBm/Hz}$ . This tells us that the added noise for the phase modulator is therefore at around  $-130 \text{ dBm/Hz}$ . This implies that the lowest power of the signal that can be measured corresponds to around  $-130 \text{ dBm/Hz}$ . The next step would be to measure a superconducting qubits system using our optical readout scheme. Typical signal strengths in the superconducting qubit experiments are about  $-125 \text{ dBm/Hz}$ . This suggests that we could potentially measure a superconducting qubit using our setup and this would be a first such demonstration of optical readout.

To reduce this gap of 65 dB, we need to use phase modulators with half wave voltages lower by 3 orders of magnitude, i.e.  $V_\pi = 10 \text{ mV}$ . Indeed there are efforts underway to make

the modulators of significantly low  $V_\pi$ . On-chip integrated modulators with compact and longer electrodes [38, 39] have been fabricated. Alternative materials such as BaTiO<sub>3</sub> [40, 41] and resonant devices [19] have been used to make modulators of lower  $V_\pi$  modulators. With more such advances, optical readout of superconducting devices could thus become a promising attempt to solve a major challenge in scalability of superconducting qubit experiments.





## 4 Conclusion and Outlook

In this master's project, I have read and understood basics of cavity electromechanics and the experimental details of its implementation. I also carried out several experiments such as optomechanically induced transparency. I carried forward the work done by previous members on design and assembly of the automatised copper filter cavities used for reducing the phase noise of the system. I wrote programs that configured how the motors on the filter cavity communicated to the measurement interface used in the lab. I investigated several algorithms to find a best way to tune the filter cavity to any desired frequency between 5-8 GHz, which is the frequency range for circuit electromechanical cavities fabricated in the lab. I was able to implement the Nelder-Mead algorithm for finding a local minimum of a function to minimize the cost function composed of errors in frequency and depth of the resonances. The implementation of this algorithm, along with the fine tuning algorithm allowed us to fit the resonances at any desired frequency with the accuracy and precision of less than 50 kHz and achieve an extinction of the input signal of around 20-30 dB. Thus the filter cavity was able to give us the reduction of the phase noise of the sources close to the shot noise level of the measurement setup. This filter cavity setup can be used in future experiments that are being planned such as observation of ponderomotive squeezing in the microwave domain, pulsed optomechanical experiments, and experiments involving the coupling of superconducting qubits to mechanical resonators.

I contributed to the ongoing experiment on the electro-optic readout of circuit electromechanical systems using a  $\text{LiNbO}_3$  electro-optic phase modulator. I took calibration measurements to estimate the amount of power reaching the EOM kept at the 3 K stage of the cryogenic dilution refrigerator. I investigated the effect of dissipation of optical power on the temperature of the phase modulator and the stage on which it was mounted. I did the calculations for measuring the  $V_\pi$  of the EOM as the temperature decreases and I measured the  $V_\pi$  of the EOM at cryogenic temperatures. I also performed a cooldown of a low  $V_\pi$  phase modulator but I observed no optical

transmission through it, implying that it did not sustain its function at low temperature. Similarly, I performed an experiment of cooling down an amplitude modulator to 3 K temperature. I also performed data transmission experiment at room temperature and cryogenic temperature. Through this experiment, our team has demonstrated the potential of the LiNbO<sub>3</sub> EOMs for applications in the optical readout of the superconducting systems such as electromechanics or qubits.

## Bibliography

- [1] M. Aspelmeyer, T. J. Kippenberg, F. Marquardt, *Reviews of Modern Physics* **2014**, *86*, 1391–1452.
- [2] H. A. Haus, *Waves and fields in optoelectronics*, Prentice-Hall, **1984**.
- [3] J. D. Teufel, T. Donner, D. Li, J. W. Harlow, M. S. Allman, K. Cicak, A. J. Sirois, J. D. Whittaker, K. W. Lehnert, R. W. Simmonds, *Nature* **2011**, *475*, 359–363.
- [4] A. Schliesser, R. Rivière, G. Anetsberger, O. Arcizet, T. J. Kippenberg, *Nature Physics* **2008**, *4*, 415–419.
- [5] L. D. Tóth, N. R. Bernier, A. Nunnenkamp, A. K. Feofanov, T. J. Kippenberg, *Nature Physics* **2017**, *advance online publication*, DOI 10.1038/nphys4121.
- [6] T. Rocheleau, T. Ndukum, C. Macklin, J. B. Hertzberg, A. A. Clerk, K. C. Schwab, *Nature* **2010**, *463*, 72–75.
- [7] M. H. Devoret, R. J. Schoelkopf, *Science* **2013**, *339*, 1169–1174.
- [8] J. M. Martinis, M. H. Devoret, J. Clarke, *Nature Physics* **2020**, *16*, 234–237.
- [9] A. Blais, S. M. Girvin, W. D. Oliver, *Nature Physics* **2020**, *16*, 247–256.
- [10] F. Arute, K. Arya, R. Babbush, D. Bacon, J. C. Bardin, et al., *Nature* **2019**, *574*, 505–510.
- [11] W. Jiang, R. N. Patel, F. M. Mayor, T. P. McKenna, P. Arrangoiz-Arriola, et al., *Optica* **2019**, *6*, 845–853.
- [12] W. Jiang, C. J. Sarabalis, Y. D. Dahmani, R. N. Patel, F. M. Mayor, et al., *arXiv preprint arXiv:1909.04627* **2019**.
- [13] J. G. Bartholomew, J. Rochman, T. Xie, J. M. Kindem, A. Ruskuc, et al., *arXiv preprint arXiv:1912.03671* **2019**.
- [14] A. P. Higginbotham, P. S. Burns, M. D. Urmey, R. W. Peterson, N. S. Kampel, et al., *Nature Physics* **2018**, *14*, 1038–1042.

- [15] M. Forsch, R. Stockill, A. Wallucks, I. Marinković, C. Gärtner, et al., *Nature Physics* **2020**, *16*, 69–74.
- [16] G. Arnold, M. Wulf, S. Barzanjeh, E. Redchenko, A. Rueda, et al., *arXiv preprint arXiv:2002.11628* **2020**.
- [17] M. Tsang, *Physical Review A* **2010**, *81*, 063837.
- [18] A. Rueda, F. Sedlmeir, M. C. Collodo, U. Vogl, B. Stiller, et al., *Optica* **2016**, *3*, 597–604.
- [19] A. Rueda, F. Sedlmeir, M. Kumari, G. Leuchs, H. G. L. Schwefel, *Nature* **2019**, *568*, 378–381.
- [20] L. Fan, C.-L. Zou, R. Cheng, X. Guo, X. Han, et al., *Science Advances* **2018**, *4*, DOI 10.1126/sciadv.aar4994.
- [21] T. P. Purdy, P.-L. Yu, R. W. Peterson, N. S. Kampel, C. A. Regal, *Physical Review X* **2013**, *3*, DOI 10.1103/PhysRevX.3.031012.
- [22] S. Probst, F. B. Song, P. A. Bushev, A. V. Ustinov, M. Weides, *Review of Scientific Instruments* **2015**, *86*, 024706.
- [23] J. A. Nelder, R. Mead, *The Computer Journal* **1965**, *7*, 308–313.
- [24] F. Gao, L. Han, *Computational Optimization and Applications* **2012**, *51*, 259–277.
- [25] T. J. Clark, V. Vadakkumbatt, F. Souris, H. Ramp, J. P. Davis, *Review of Scientific Instruments* **2018**, *89*, 114704.
- [26] R. W. Boyd, *Nonlinear optics*, Academic press, **2003**.
- [27] C. Herzog, G. Poberaj, P. Günter, *Optics Communications* **2008**, *281*, 793–796.
- [28] J. D. Morse, K. G. McCammon, C. F. McConaghy, D. A. Masquelier, H. E. Garrett, et al. in *Design, Simulation, and Fabrication of Optoelectronic Devices and Circuits, Vol. 2150*, (Ed.: M. N. Armenise), International Society for Optics and Photonics, SPIE, **1994**, pp. 283–291.
- [29] C. McConaghy, M. Lowry, R. Becker, B. Kincaid, *IEEE Photonics Technology Letters* **1996**, *8*, 1480–1482.
- [30] K. Yoshida, Y. Kanda, S. Kohjiro, *IEEE Transactions on Microwave Theory and Techniques* **1999**, *47*, 1201–1205.
- [31] E. D. Black, *Am. J. Phys* **2001**, *69*, 79–87.
- [32] S. Weis, R. Riviere, S. Deleglise, E. Gavartin, O. Arcizet, et al., *Science* **2010**, *330*, 1520–1523.

- [33] X. Zhou, F. Hocke, A. Schliesser, A. Marx, H. Huebl, et al., *Nature Physics* **2013**, *9*, 179–184.
- [34] A. H. Safavi-Naeini, T. M. Alegre, J. Chan, M. Eichenfield, M. Winger, et al., *Nature* **2011**, *472*, 69–73.
- [35] J. D. Teufel, D. Li, M. S. Allman, K. Cicak, A. J. Sirois, et al., *Nature* **2011**, *471*, 204–208.
- [36] F. Marquardt, J. Harris, S. M. Girvin, *Physical Review Letters* **2006**, *96*, 103901.
- [37] T. Carmon, H. Rokhsari, L. Yang, T. J. Kippenberg, K. J. Vahala, *Physical Review Letters* **2005**, *94*, 223902.
- [38] C. Wang, M. Zhang, X. Chen, M. Bertrand, A. Shams-Ansari, et al., *Nature* **2018**, *562*, 101–104.
- [39] S. Manipatruni, K. Preston, L. Chen, M. Lipson, *Optics express* **2010**, *18*, 18235–18242.
- [40] S. Abel, F. Eltes, J. E. Ortmann, A. Messner, P. Castera, et al., *Nature Materials* **2019**, *18*, 42–47.
- [41] F. Eltes, G. E. Villarreal-Garcia, D. Caimi, H. Siegwart, A. A. Gentile, et al., *arXiv:1904.10902 [physics]* **2019**, arXiv: 1904.10902.